Applied Catalysis B: Environmental 291 (2021) 120068

Contents lists available at ScienceDirect

Applied Catalysis B: Environmental

journal homepage: www.elsevier.com/locate/apcatb

Effects of the induced micro- and meso-porosity on the single site density and turn over frequency of Fe-N-C carbon electrodes for the oxygen reduction reaction

Marco Mazzucato [a], Giorgia Daniel [a], Asad Mehmood [b], Tomasz Kosmala [a], Gaetano Granozzi [a], Anthony Kucernak [b], Christian Durante [a,*]

[a] Department of Chemical Sciences, University of Padova, via Marzolo 1, 35131, Padova, Italy
[b] Department of Chemistry, Imperial College London, South Kensington, SW7 2AZ, London, UK

ARTICLE INFO

Keywords:
ORR
Fe-N-C
Single site catalyst
Electrocatalysis
Fuel cell

ABSTRACT

Fe-N-C have emerged as one of the best non-PGM alternatives to Pt/C catalysts for the electrochemical reduction of O_2 in fuel cells. In this work, we explore the effect of steam and CO_2 treatments at high temperatures on the nanometric porous structure of a commercial carbon black. Using those support materials, we synthesize different Fe-N-C catalysts to achieve a better understanding on the role of micro- and mesopores of the support towards catalytic site formation and site activity. Different time and temperature of treatments result in an almost linear increment of surface area and microporous volume, which allows better nitrogen functionalization. Site density evaluation, performed using a recently described NO-stripping technique, showed an increase in site density and TOF which correlates well with the morphology variation. The percentage of active iron increases from 2.65 % to 14.74 % in activated catalysts confirming a better access of electrolyte to the iron sites.

1. Introduction

It is nowadays well recognized that the commercialization of proton-exchange membrane fuel cells (PEMFCs) is highly hindered by the cost of the cathode side catalyst layer which is commonly manufactured using Pt/C. For this reason, great efforts have been and continue to be made in order to find alternatives [1]. The two main classes of material that have been explored for the oxygen reduction reaction (ORR) are low-content Pt catalysts and Platinum Group Metals (PGM)-free catalysts. The first route aims at producing highly active and durable (layer stability and poisoning resistance) catalysts in order to reduce the amount of Pt needed to run the cell efficiently and to improve the life of the devices [2]. Different approaches have been adopted, e.g. creation of Pt alloys with transition or late earth metals [1,3–6] and/or by engineering of nanoparticles (NPs) size and shape [7,8], focusing also on the interaction with the support, commonly pristine or doped carbon [9–11]. The second PGM-free route aims at finding materials with good activity and durability based on cheap and earth-abundant metals. Within the PGM-free group, the metal-nitrogen-doped (M-N-C) materials have emerged as the most promising candidate [12–15] due to the low cost [16,17] and their performances which are slowly approaching those of Pt-based materials, in particular in alkaline environment [18]. Among all M-N-C materials, Fe-N-C has become the most studied and promising system due to the good activity and stability if compared with other metal center like Co, Mn, or Zn [19]. However, the nature of the active sites in these catalysts is still under debate [20–22]; in addition, the role of the support, of the doping precursor and of the synthesis condition on the final system in term of activity and type of sites formed still have to be fully rationalized.

Combining multiple spectroscopic technique and DFT computational analysis [22–24] it is progressively emerging that the main active sites in Fe-N-C materials are the Fe-N_x centres with the assistance of C-N functionalities (such as pyrrolic, pyridinic and graphitic nitrogen) and, perhaps through other co-catalyst centres such as Fe/Fe_3C or less likely FeO_x NPs encapsulated by few layers of N-doped carbon that could change the local electronic density [23,25–31]. Such evidences were confirmed both by comparison of similar catalysts made with and without iron addition, but also by specifically poisoning the metal sites [32] with different chemical moieties like CN^-, SCN^- [21,33], NO [34], CO [35], NO_2^- [36], the last two also allowing quantitative analysis.

* Corresponding author.
E-mail address: christian.durante@unipd.it (C. Durante).

https://doi.org/10.1016/j.apcatb.2021.120068
Received 16 November 2020; Received in revised form 5 February 2021; Accepted 13 February 2021
Available online 28 February 2021

A carbonaceous pre-synthesized support or metal-doped carbon materials prepared starting from nitrogen-based chelating centers or metal complexes are the building blocks for some recent catalysts [37,38]. Other synthetic strategies start from very cheap precursors, e.g. biomass, waste plastic or polymers, that allow formation of different porous supports, even with nitrogen or sulphur doping [17,39,40]. An example of a recently developed strategy is to use metal-organic framework (MOF) highly porous structures (namely a zinc based one, ZIF-8) as precursors of C and N to selectively form M-N_x centres and, at the same time, obtaining highly accessible active sites [22,41,42]. It turns out that the M-N_x structure is maintained even after the pyrolytic step, which is a standard procedure adopted for these types of material [43]. Multi-step synthesis is another important approach that considers a double thermal treatment interspersing an acid wash for the removal of inorganic species. This synthetic protocol is proven to be useful for increasing activity thanks to the opening of porous structure clogged by inorganic species, yielding a higher density of accessible sites [44–46]. This last approach will be also adopted in this work.

One common feature of all these approaches is the attention to specific surface area and porous structure of the support (micro-, meso- and macropore ratio) because these are fundamental for the formation of metal-nitrogen active sites, and for the transport of reactants and products [47,48]. Regarding the last aspect, the present study aims at understanding and confirming the role of micro- and mesopore on catalytic sites formation. In particular, controlled activation treatment has been performed on a commercial carbon black with low surface area (S $\sim$ 60 m^2 g^{-1}) in order to progressively raise the surface area (and the pore volume). This, in turn, is expected to enhance the catalytic site density and site accessibility. The importance of micropores has been already singled out [49,50], where the combination of several techniques was employed to locate the presence of Fe-N_x sites in micropores and mesopores. However, the systematic variation of the catalyst textural properties and the determination of the site density by an innovative NO-stripping technique allowed us to attain a direct evidence of how site density and turn over frequency of a Fe-N-C catalyst are connected with micro and mesopore volume and surface area. A detailed physico-chemical and electrochemical characterization was carried out to relate morphological properties of the support with the final activity of the catalysts.

2. Experimental

2.1. Activation treatments

The setup for the activation treatments consisted of a tubular furnace (Carbolite, with a quartz tube Ø =55 mm) flanged at both sides to control the inner atmosphere. The outlet flange was connected to the purging line directed to a scrubber, whereas the inlet flange was connected to the N_2 mass flow control. The inlet flange also lodged a stainless steel needle, which was connected to a syringe pump (SKE Research Equipment) and positioned so that the needle tip laid at the entrance of the oven. The syringe pump was actioned after purging the tubular furnace with N_2 and once the temperature reached the targeted temperature (950 °C). The syringe pump injected milli-Q water at 1 mL min^{-1}, achieving the almost instantaneous water evaporation. A certain amount of carbon black (CB) (Super P®) was placed in the furnace with a 100 sccm N_2 flow (controlled by a PR4000B massflow, mks instrument) at 25 °C for 90 min and then heated up to 100 °C for 1 h to remove moisture and oxygen. The temperature was then raised to the final temperature with a rate of 5 °C min^{-1}. Once the set temperature was reached, the nitrogen flow was reduced to 50 sccm. The starting CB (hereafter referred to as CBSt-X where X = treatment time in min.) was treated for a period in the range 10–60 minutes, and then cooled down to ambient temperature within a 50 sccm N_2 flow.

Carbon dioxide activation was carried out with the same procedure with the only difference that, once the targeted temperature of 950 °C was reached, the nitrogen flow was replaced by a flow of CO_2 of 100 sccm. The pristine CB was treated for a period in the range 1–9 h (hereafter referred as CBCO_2-W where W = treatment time in hour), and then cooled down to ambient temperature with a 50 sccm N_2 flow. To evaluate the role of temperature, other treatments have been carried out at 850 °C and 1050 °C maintaining a constant exposure time of 5 h. These last samples were named as CBCO_2-5-Y (where Y is the temperature in °C).

All the obtained samples were vibro-milled (Retsch MM 400, 10 mL, and 5 mL steel jars with steel balls) obtaining a micrometric powder to facilitate further treatments or characterization.

2.2. Synthesis of Fe-N-C materials

Iron(II)-phenanthroline chloride (hereafter referred to as Fe$(Phen)_3Cl_2$), was synthesized from anhydrous $Fe^{II}Cl_2$ and 1,10-phenantroline in ethanol according to literature (see SI for specification) [17]. The synthesis of Fe-N-C catalysts were carried out as follow: 200 mg of CB or the activated carbon and 222 mg of $Fe(Phen)_3Cl_2$ (equivalent to the 2 $\%_{molar}$ of iron compared to the molar amount of carbon) was vibro-milled at 18, 20 and 25 Hz for 1 h (20 min. for each frequency in ascending order), then heated at 900 °C in a tubular furnace (Carbolite, with a quartz tube Ø =25 mm) for 2 h under nitrogen-hydrogen atmosphere (9% H_2 in the mixture, HG 2400 Claind) and eventually cool down to ambient temperature under pure nitrogen flow. The resulting powder was vibro-milled and then washed at reflux in 100 mL 1 M solution of H_2SO_4 for 3 h at 100 °C under continuous stirring and then filtered and rinsed with at least 0.5 L of milli-Q water and finally dried in oven at 40 °C overnight. After the acid leaching, the powder was vibro-milled a second time and then heated again at 900 °C as described before. The resulting powder, labelled as FNCBSt-X, FNCBCO_2-W or FNCBCO_2-5-Y (where X and W are the treatment time in min. and hours, respectively and Y is the temperature treatment) are the final catalyst. The sample obtained from the non-treated CB was labelled as FNCB. This procedure allows to obtain more or less 200 mg of catalyst. The catalysts were vibro-milled another time before electrochemical test with the same settings listed above. Other iron molar percentage were also prepared, i.e.1% and 4%, which however resulted in less active ORR catalysts with respect to the 2 $\%_{molar}$ one (Fig. S2).

2.3. Electrochemical test

Cyclic voltammetry (CV) and linear sweep voltammetry (LSV) were carried out on a rotating ring-disc electrode (RRDE, Metrohm; ∅ =5 mm GC disk and a Pt ring), in both Ar-purged and O_2-saturated 0.5 M H_2SO_4 solution using an Autolab model 101 N potentiostat. All measurements were done in a three-electrode cell thermostated at 25 °C. The RRDE tip was used as working electrode, a graphite rod was used as counter-electrode and a homemade RHE as reference electrode prepared before each experiment according to literature [5]. It consists in a spiral Pt wire settled to the closed end of a capillary glass tube filled with the electrolyte solution in which H_2 was directly electrogenerated at the Pt wire via chronoamperometric technique until half of the spiral was filled with gas.

The materials activity was investigated on a thin catalyst layer loaded on GC surface via drop-casting after the preparation of an ink made approximately of a 9:1 mixture of water, an organic solvent (acetone and THF) and Nafion ($m_{cat}/m_{nafion\ solution} \approx 1$). To obtain a good dispersion the ink was sonicated both in a bath and probe sonicator. The loading was chosen to be 0.6 mg cm^{-2} as used in previous work [17], other loadings were also tested as discussed later in the text (see also Fig. S6).

All the materials were initially activated in Ar-purged electrolyte with extensive CV cycling at 200 mV s^{-1} until a stable current was observed. In ORR tests, O_2 was bubbled inside the electrolyte solution for at least 30 min. The number of transferred electron (n) was

determined by RRDE linear sweep voltammetry according to the following equation (Eq. 1):

$$n = \frac{4|i_D|}{|i_D| + |i_R|/\mathrm{N}} \quad (1)$$

Where i_D is the current recorded at disk, i_R the current recorded at ring and N the collection efficiency, which is equal to 0.25 (determined by performing RRDE measurement in the presence of $K_4Fe(CN)_6$ in 0.5 M K_2SO_4 electrolyte) [51]. With the last analysis it is also possible to evaluate the percentage of hydrogen peroxide (Eq. 2) produced at the working electrode:

$$\%_{H_2O_2} = 100 \cdot \frac{4-n}{2} = \frac{100 \cdot 2|i_R|}{N \cdot |i_D| + |i_R|} \quad (2)$$

Other parameters of interest are the peak potential (E_p) derive from the CV recorded in oxygen saturated electrolyte at 5 mV s^{-1}, the half-wave potential ($E_{1/2}$), and the limiting current density (j_{lim}) determined from LSV analysis at 2 mV s^{-1} and 1600 rpm. The mass-transport corrected kinetic current density at a selected potential was calculated according to Eq. (3).

$$j_{k,E} = \frac{j_{lim} \cdot j_E}{j_{lim} - j_E} \quad (3)$$

where j_E is the current density at the selected potential $E = 0.8$ V vs RHE.

To evaluate the catalysts site density, nitrite (NO_2^-) poisoning and electrochemical stripping were performed following the procedure described by Malko et al. [36]. This procedure allows the selective poisoning of Fe-N_x site and the site density is determined by measuring the charge of NO reductive stripping during a CV measurement. The site density measurements were performed on a thin layer of catalyst deposited on a GC (RDE, PINE Research Ø =5 mm) in a 0.5 M acetate buffer at pH 5.2. A loading of 0.2 mg cm^{-2} was chosen according to published procedure, the ink was let dry with the electrode in rotation at 130 rpm for about 20 min. These measurements were carried out on SP-300 Biologic instrument equipped with linear cyclic voltammetry scansion (CVL) module.

Stability tests were performed following the current variation when a constant potential of 0.15 V vs. RHE was applied. The potential, which coincides with a mass transfer limiting condition was hold for 9 h except for a small period every 3 h used for recording a LSV to evaluate the variation of activity in term of half-wave potential. All measurements were performed in O_2-saturated electrolyte 0.5 M H_2SO_4 at a rotation speed of 200 rpm and controlled temperature of 25 °C. The loading was 0.6 mg cm^{-2} on a 5.5 mm glassy carbon RDE, reference electrode was a saturated mercury sulfate (0.64 V vs. NHE) and the counter electrode was a graphite rod.

2.4. Physico-chemical characterization

X-ray photoemission spectroscopy (XPS) measurements were performed at room temperature in a UHV chamber (base pressure $< 5 \cdot 10^{-9}$ mbar), equipped with a double anode X-ray source (Omicron DAR-400) and a hemispherical electron analyzer (Omicron EIS-125). A non-monochromatized Mg-Kα radiation ($h\nu$ = 1253.6 eV) and pass energies of 50 eV and 20 eV for the survey and the single spectral windows, respectively, were used. The calibration of the Binding Energy (BE) scale was carried out using Au $4f_{7/2}$ as a reference (BE Au $4f_{7/2} = 84.0$ eV). The XPS peak of nitrogen was deconvoluted into single components by using symmetrical Voigt functions.

Raman spectra were recorded using a micro-Raman set-up with a 1 mW laser at 532 nm with 50xLWD objective (pinhole 25 μm). N_2 adsorption/desorption isotherm were recorded at 77.3 K using an ASAP 2020 Plus instrument. Specific surface area of the samples was determined by BET analysis and with Quenched Solid Density Functional Theory (QSDFT) model, which showed to be more accurate compared to NLDFT, even if limited to pore dimension of 40 nm. In fact, it takes into account the roughness of the surface and chemical heterogeneity leading to a better fit of experimental data, in particular for disordered carbons [52,53]. Pore size distribution was determined using a slit pore model because it allows a better fit to the experimental data (a comparison between different models is reported in Fig. S1). The total volume of pore was obtained applying Gurvitsch law at $p/p^\circ \approx 0.98$. Elemental analysis (EA) was carried out using a Thermo Scientific Flash 2000 analyzer. Transmission electron microscopy (TEM) images were obtained with a FEI TECNAI G2 instrument operating at 100 kV.

3. Result and discussion

3.1. Carbon supports activation and characterization

The Super P® Conductive CB was chosen as starting carbon material because of the relatively low surface area (66 $m^2\ g^{-1}$) and a comparable micropore and mesopore area (Table 1). The CO_2 activation treatment was carried out at 950 °C from 1 h to 9 h obtaining a burn-off of about 25 %, which is reasonable considering that the starting material has a medium-high degree of graphitization (see Raman analysis later in the text) [54,55]. The isotherms obtained by physisorption of N_2 at 77.3 K for samples treated with CO_2 at different exposure times are reported in Fig. 1 while data are listed in Table 1. The isotherms change from a hybrid I-II type with a very small hysteresis for the pristine CB sample, indicating a starting material made of macropore with a small amount of micro and mesopore, to isotherms with H3/H4 type hysteresis for the activated CBs (Fig. 1a). The growing of initial uptake at low relative pressure indicates an evolution of micro and mesopore (Fig. 1d), whereas the steep uptake at high relative pressure indicate that also macropores are evolving. The appearance of this type of hysteresis is also related to slit-shaped pores, supporting the choice of the DFT model [56,57]. The characteristic hysteresis closure at relative pressure of about 0.45 is generally due to cavitation [57].

The effect of carbon dioxide activation is generally described as an opening of narrow micropores followed by widening due to the reaction $C + CO_2 \rightarrow 2CO$ enhanced by the oxidizing behavior of CO_2 in the 800−1000 °C range of temperature [58–60]. The actual mechanism is not well understood, and the phenomenon could occur in different steps; furthermore the surface chemistry of the CB (oxygen and hydrogen content) can impact on the reactivity [61] and the actual flow of CO_2 can impact on the final result. Usually, for high temperature a low flow is

Table 1
Textural properties and elemental analysis of activated CB supports.

	EA[a]		S[b]	S_μ[c]	S_{meso}	V_μ[c]	V_{meso}	V_{tot}[d]
	%C	%H	$m^2\ g^{-1}$	$m^2\ g^{-1}$	$m^2\ g^{-1}$	$cm^3\ g^{-1}$	$cm^3\ g^{-1}$	$cm^3\ g^{-1}$
CB	98.75	0.17	66	35	31	0.015	0.137	0.204
CBSt-10	85.86	0.12	186	129	57	0.058	0.365	0.767
CBSt-20	98.81	0.12	257	182	75	0.081	0.432	0.923
CBSt-30	97.29	0.17	303	202	101	0.092	0.485	0.982
CBSt-60	97.29	0.17	531	318	213	0.146	0.742	1.108
CBCO$_2$-1	98.87	0.06	100	63	37	0.027	0.200	0.368
CBCO$_2$-5	98.23	0.24	197	129	68	0.055	0.457	0.791
CBCO$_2$-9	98.08	0.08	258	168	90	0.076	0.456	0.969
CBCO$_2$-5-850	96.79	0.10	106	59	47	0.024	0.355	0.719
CBCO$_2$-5-950	98.23	0.24	197	129	68	0.055	0.457	0.791
CBCO$_2$-5-1050	97.33	0.10	381	237	144	0.108	0.580	0.903

[a] elemental analysis by CHNS elemental analyser.
[b] QSDFT slit method 0.5−40 nm.
[c] pore width < 2 nm.
[d] obtained by applying Gurvitsch law at $p/p^\circ \sim 0.98$.

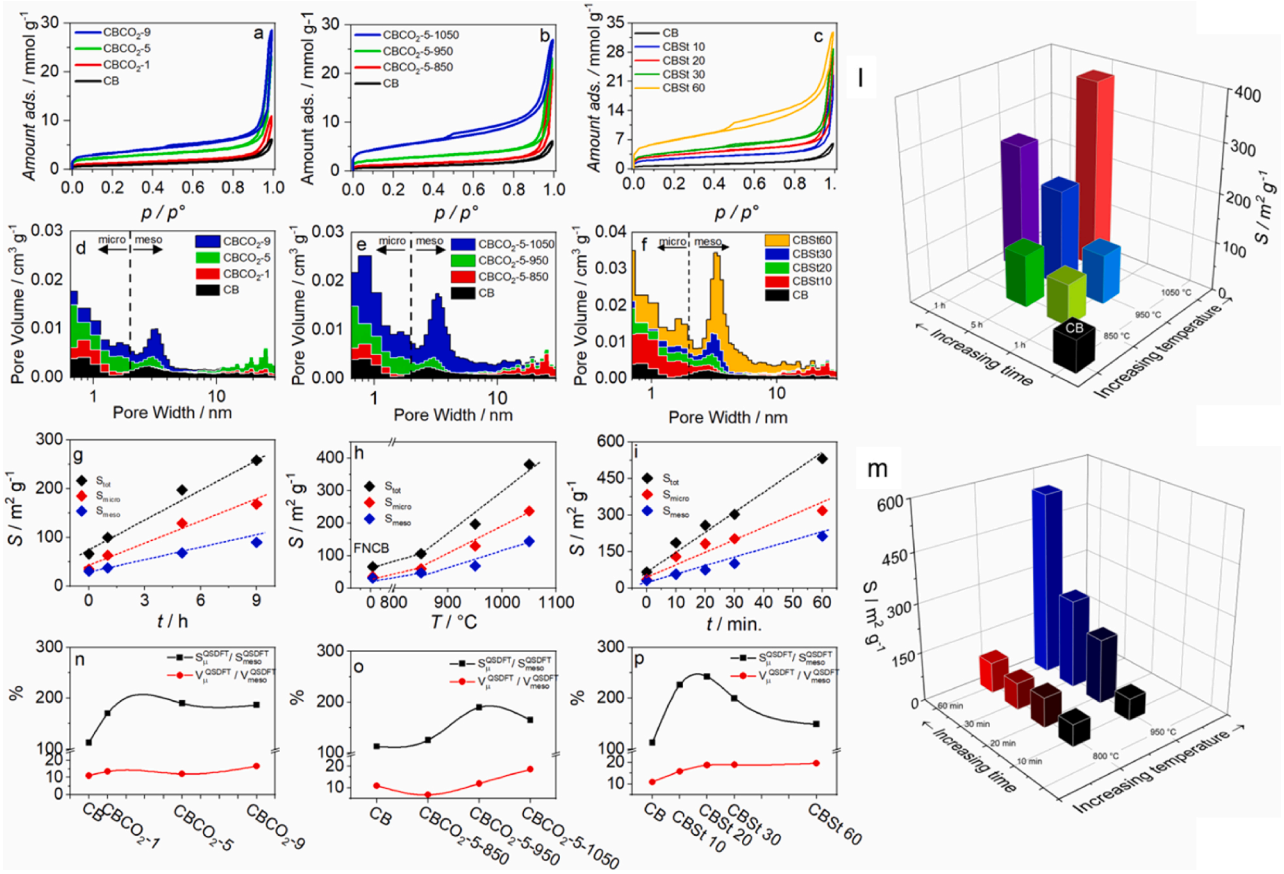

Fig. 1. (a–c) N_2 adsorption isotherms and (d-f) pore size distribution for CO_2 treatment at (a,d) fixed temperature varying the exposure time and (b,e) fixed exposure time of 5 h and different temperature and (c,f) steam treatment at different exposure time; (g-i) surface area and surface of mesopore and micropore with respect to time and temperature of activation treatment; Combined effect of time and temperature in (l) CO_2 treatment and (m) steam treatment; Micro and mesopore surface area and volume ratio for (n,o) CO_2 treatment; (p) steam treatment.

preferable [62]. In our case it was possible to observe a general evolution of the surface area (Fig. 1a–b), initially due to the evolution of micropore that for longer treatment is also accompanied by the development of mesoporosity and macroporosity.

Increasing CO_2 treatment time produces a linear evolution of surface area (~ 260 $m^2\ g^{-1}$ for 9 h) with a slightly preferential evolution of micropore accompanied by an evolution of mesopore due to a widening effect (Fig. 1d,g). Fig. 1d report the evolution of pore dimensions and it is evident that the CO_2 treatment mostly increases the pore volume while keeping the pore diameter almost unchanged. This can be explained considering either the opening of new pores or the elongation of those already existing. To accelerate the activation process, CO_2 treatment at higher temperatures were also carried out. As expected, the carbon support surface area increases upon increasing the treatment temperature (from 850 °C up to 1050 °C) while the treatment duration was kept constant at 5 h (Fig. 1b). The isotherm of sample treated at 1050 °C shows a more pronounced H3/H4 type hysteresis. This result is in line with the endothermic nature of the reaction, which is actually one of the reasons why steam and CO_2 are preferred for activation instead of air [54]. Also, in this case pore diameters change only slightly, whereas the pore volume increases consistently (Fig. 1e). From Fig. 1h, it is clear that the surface area increases almost linearly with the temperature and from data in Table 1 it is possible to conclude that an increment of 100 °C in the set temperature from 950 °C to 1050 °C is more effective than the increment of 4 h at 950 °C (from 5 h to 9 h). The histogram in Fig. 1l resumes the effect of time and temperature on the increment of the surface area, and it is well evident that the increment of temperature is more effective.

The N_2 adsorption isotherms for the samples activated with steam at high temperature are reported in Fig. 1c. The isotherms evolve from a hybrid I-II type of CB with a very small hysteresis to a pronounced H3/H4 hysteresis loop of CBSt-60, which indicates an evolution of micro and to a more extent of mesopore as observed also for the CO_2 treatments. The action of steam is generally described as different when compared with that of CO_2. In fact, a general enlargement of existing pores is expected leading to larger pore size distribution. However in this case more reaction could be involved: [63]

$$C + H_2O \rightleftharpoons H_2 + CO \quad (4)$$

$$C + 2H_2O \rightleftharpoons 2H_2 + CO_2 \quad (5)$$

$$C + CO_2 \rightleftharpoons 2CO \quad (6)$$

$$CO + H_2O \rightleftharpoons CO_2 + H_2 \quad (7)$$

Therefore, CO_2 is also generated *in situ* (behaving as an activating agent), so explaining why a broader pore distribution is expected with this treatment. What it is indeed observed is a slightly preferential widening of mesopore of various dimension, in particular for the longer treatment (60 min) and a consistent gain in volume. Nevertheless, a peak around 4−5 nm arises, probably due to the opening of existing pore of 2−3 nm in the pristine CB, as visible in the histogram in Fig. 1f. This confirms that both opening and widening/elongation effects are present. From Fig. 1i, it is clear that the micro, meso and total surface areas increase almost linearly with the time of exposure. It is important to stress that the steam treatment is much more effective at 950 °C than at 800 °C as evidenced in Fig. 1m, where the effect of time exposure is also reported. Furthermore, steam treatment is much more effective than the CO_2 one, since almost the same textural values are obtained with a 20

min steam treatment compared to a 9 h CO_2 treatment at the very same temperature.

Summarizing we were able to prepare different CB supports starting from a low surface area one, where a significant and fast improvement in pore volume is achieved with steam, while with CO_2 a more controlled evolution is possible. Fig. 1n and p show the relation between time of treatment and micropore-mesopore volume and surface ratio (pore width 0.5 ÷ 40 nm) for CBs treated with both steam and carbon dioxide. In addition, Fig. 1o shows the same relation but considering the effect of increasing temperature in CO_2 treatment. The two trends appear to be similar for both steam and CO_2 treatments, where an initial growing of micropore is reasonably caused by opening of new pore, while longer treatment brings a plateau meaning that new pores are formed but also existing pores are widened or elongated (Fig. 1n and p). The enhancement of the temperature of the CO_2 treatment seems also to affect mostly the micropore evolution (Fig. 1o). The apparent discordance between volume ratio and surface ratio is certainly a consequence of the geometry of pores and their dimension: larger pores have a smaller surface to volume ratio. It is worth noting that for the whole set of data, micropore volume increases linearly with micropore area, whereas a second order relation links the mesopore volume with the mesopore surface area. This can be explained considering that both steam and CO_2 treatments leads to an elongation of the pore rather that their widening. Conversely the action of both treatments on mesopore is to both enlarge and elongate the pre-existing pores. We mention here that also a slit/cylindrical adsorption branch model gives a good fit with a similar distribution (Fig. S1). Probably some deeper cylindrical pores or wedge-like shaped pores might form, but obviously we do not know the actual shape considering that the synthesis is not done with a templating agent and that the type of measurement gives only an average description. Considering these things and looking at some literature works [64,65], we chose to maintain the same model (slit) for all samples. Elemental analysis showed no significant changes in carbon support composition, with the sole exclusion of the anomalous CBSt-10. It is our impression that CBSt-10 contains a higher content of oxygen and that the steam treatment produces an increased number of oxygen functional groups, which form at the beginning of the treatment and are oxidized to CO_2 after prolonged treatments.

In order to evaluate the possible effects of degree of graphitization, Raman characterization was also performed on all samples (Fig. 2a). The spectra were deconvoluted with 5 bands (Fig. 2b) in the region between 1100 and 1700 cm^{-1} [66–69] as described in Table S1 after a normalization relative to the G band peak (namely to the Raman shift around 1600 cm^{-1} for which the maximum intensity is recorded [70]). In the region between 2200 and 3200 cm^{-1}, 2 or 3 bands were used to deconvolute the spectrum according to Sadezky et al. [68] This spectral region is generally called the graphene/graphene oxide region because at least two distinct bands similar to those of graphene oxide are observed in materials such as CB (Fig. 2a). The similarity comes from the aromatic region with non-oxidized benzene rings and the regions containing C—OH, epoxide and double bonds [68,71–73]. We do not report the deconvoluted data because no evident trend was observed. No

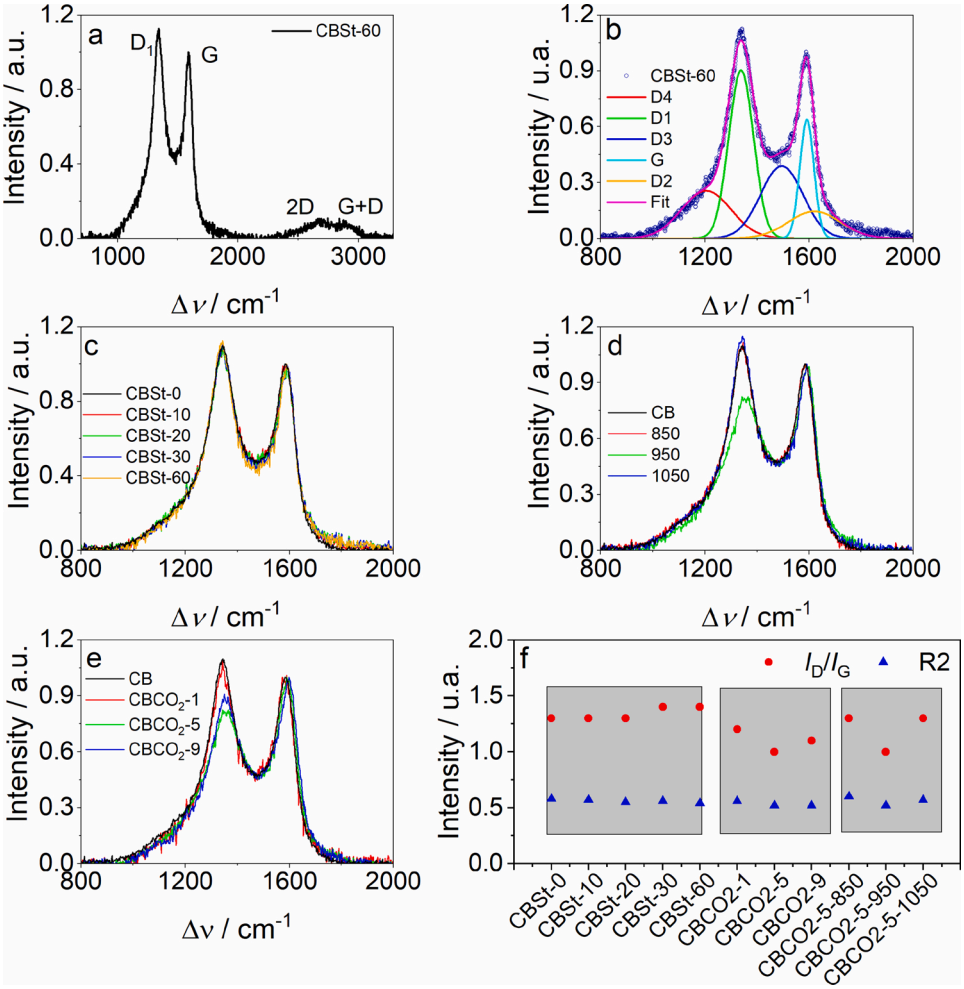

Fig. 2. a) full range Raman spectrum for CBSt-60; b) example of Raman spectrum deconvolution; Overlay of spectra acquired in different activation condition c) steam; d) CO_2 treatment at different temperature for 5 h; e) CO_2 treatment at different exposure time; f) I_d/I_g ratio variation within single set of activated carbons and R2 values.

particular changes were neither observed in I_G/I_{D1} ratio or in G band position upon steam treatment (Fig. 2c and f), only a slight change in graphene/graphene oxide band in the region 2400 ÷ 3000 cm^{-1} was observed when comparing CBSt-60 with the pristine CB. More evident changes were observed for carbon dioxide treatment (Fig. 2d,e), in particular the I_G/I_{D1} ratio and the G band position slightly changed (Table S2), though without a clear trend, and the evident the decreasing of the D1 band intensity for sample treated at 950 and 1050 °C. This behavior is in agreement with the raising of graphitization degree in the material [66,74]. For poorly organized carbon materials R2 > 0.5, while a R2 < 0.5 is indicative of highly graphitized carbons, where R2 = D1/(G + D1 + D2) is the ratio between the area of D1 peak and the sum of G, D1 and D2 areas (Table S2 and Fig. 2f). In the present case the R2 parameter slightly decreases after prolonged CO_2 or steam treatment or increasing the temperature, confirming a reasonable increase of graphitization. [75]

3.2. Synthesis and characterization of Fe-N-C catalysts from CB activated supports

All the Fe-N-C catalysts where prepared by thermal treatment of activated CBs and $Fe(Phen)_3Cl_2$ at 900 °C according to a procedure described in the experimental section.

The optimal amount of iron-phenanthroline used for the formation of Fe-Nx active sites in the final catalyst was defined by evaluating the effect of different initial amounts on the resultant catalyst ORR activity. The selection was made by adopting $CBCO_2$-5 and four different $Fe(Phen)_3Cl_2$ molar concentrations i.e. 0, 1, 2 and 4 $\%_{mol}$. According to the elemental analysis reported in Table S3, the maximum amount of nitrogen was obtained for the 2% sample. The LSV for ORR measurements and the correlation between the iron percentage and activity are reported in Fig. S2: the sample with 2% of iron shows the best compromise between activity and precursor quantity. In fact, the 4% sample was only slightly better in term of activity, but considering that a similar activity is obtained with half of the iron, the 2% one represents a better choice. Therefore, all the activated CBs were functionalized by adopting 2$\%_{mol}$ of $Fe(Phen)_3Cl_2$ compared to the amount (molar) of carbon support.

Elemental analysis confirms the nitrogen presence in all the prepared catalysts (Table 2). Interestingly, the weight percentage concentration grows by one order of magnitude on going from 0.1 % in FNCB to 1.06 % in FNCBSt-30 and to 0.9 % for $FNCBCO_2$-5 (Table 2). However, it is bizarre to see that the most porous sample of each set shows a small decrement in nitrogen content. This might suggest that the percentage around 1% of nitrogen is the maximum obtainable with these support materials under the adopted synthetic conditions.

Fig. 3 shows TEM images of the investigated catalysts obtained from different activated supports. Sorting through the images of the steam activated catalysts, there are no evident changes in CBs particle size, which remains in the range of 40−80 nm as for the pristine CB particles. More evident is the morphology variation, since the activated CBs becomes progressively more porous and less dense on passing from zero to 60 min of steam treatment (Fig. 3a–e). Very few isolated iron NPs enveloped in a carbon shell are also visible whereby a protection on iron particles can be expected so enhancing the corrosion resistance and the stability of the catalysts also in the very demanding pH condition employed for the acidic wash. The CO_2 activated Fe-N-C samples are reported in Fig. 3f–j. Also in this case, there is no evident change in the particles dimension, while some shell-like nanoparticles and some nanotube like structure containing Fe NPs could be observed. In general, these samples do not show a large quantity of Fe NPs, in good agreement with the low content of surface iron derived from the XPS analysis (vide infra).

The Fe-N-C surface composition was investigated by a comprehensive XPS analysis, which evidenced the surface presence of iron, oxygen, carbon and nitrogen. The maximum nitrogen surface content is limited to ca. 1 % (in $FNCBCO_2$-9 and $FNCBCO_2$-5-850, see Table 2), as already evidenced from the bulk elemental analysis; the N 1s peak was fitted with 6 components (Figs. 3a and S3) i.e. imine N (397.8 eV), pyridinic N (398.8 eV), Fe-N_x (399.9 eV), pyrrolic N (400.7 eV), graphitic N (401.7 eV) and N–O group (402.7 eV). [12,13] The low N content (< 1%, close to the XPS detection limit) suggests to take with caution the deconvoluted data. Actually, the data show an apparent increment of pyridinic and pyrrolic nitrogen, but a diminution of Fe-N_x (apart from the $FNCBCO_2$-9 sample, see Fig. 4d–f and Table 2). This last finding was unexpected considering that several works in literature claim the fundamental role of microporosity for the iron-nitrogen center formation and therefore Fe-N_x were expected to increase moving from pristine to activated carbons showing a significant higher content of micropores. [50,76] However, it is possible that Fe-N_x sites are possibly formed and hosted in the NC matrix generated from the pyrolysis of 1,10-phenanthroline which may stay at the surface of those preformed CB supports, but even in this case a decrement is not expected. It is also true that the formation of Fe particles, subsequently removed by acid leaching, may depend on the surface properties of CB supports which would in turn change the amount of Fe-N_x sites. It is noteworthy that the FNCB sample, which has the lowest content of bulk nitrogen according to the elemental analysis, has on the other hand the highest concentration of surface nitrogen (Table 2). This is reasonable assuming that in the untreated support shallow pores are present, while in more porous sample some nitrogen could be confined inside pores undetectable by XPS but still electrochemically accessible. For this reason, we retain that XPS measurements are helpful to characterize different nitrogen sites in non-porous samples, while it has some limits to determine bulk N sites in highly porous samples, in particular when the nitrogen content is too

Table 2
Elemental analysis and XPS data deconvolution.

	EA [a]			XPS [b]				N 1 s deconvolution [c]					
	%C	%N	%H	C 1 s	O 1 s	N 1 s	Fe 2p	N_{Iminic}	$N_{Pyridinic}$	$N_{Fe\text{-}Nx}$	$N_{Pyrrolic}$	$N_{Graphitic}$	$N_{N\text{–}O}$
FNCB	95.91	0.10	0.24	91.52	7.04	1.03	0.41	11.2	15.9	22.3	22.6	19.3	8.7
FNCBSt-10	88.18	0.74	0.43	90.54	8.25	0.80	0.41	10.5	19.2	23.6	23.8	14.3	8.6
FNCBSt-20	91.46	0.87	0.30	92.37	6.26	0.91	0.46	10.9	24.5	13.1	27.9	14.1	9.5
FNCBSt-30	91.23	1.06	0.32	92.58	6.01	0.91	0.50	12.2	21.0	18.1	29.7	16.0	3.0
FNCBSt-60	92.11	0.84	0.33	93.58	5.51	0.64	0.27	8.8	23.9	15.4	31.4	13.7	6.8
$FNCBCO_2$-1	87.32	0.52	0.28	90.45	8.40	0.78	0.36	15.2	21.0	19.8	28.2	12.3	3.5
$FNCBCO_2$-5	95.75	0.90	0.25	92.34	6.79	0.59	0.27	19.8	27.2	17.3	30.3	5.4	0.0
$FNCBCO_2$-9	92.28	0.77	0.29	87.74	10.51	1.12	0.63	11.5	22.4	24.0	26.3	9.0	6.8
$FNCBCO_2$-5-850	91.53	0.50	0.37	86.14	11.78	1.23	0.85	14.2	31.7	14.0	29.0	11.1	0.0
$FNCBCO_2$-5-950	95.75	0.90	0.25	92.34	6.79	0.59	0.27	19.8	27.2	17.3	30.3	5.4	0.0
$FNCBCO_2$-5-1050	95.07	0.74	0.27	91.73	7.38	0.71	0.18	17.0	30.1	15.7	25.9	11.3	0.0

[a] elemental analysis by CHNS elemental analyser.
[b] surface chemical composition from XPS measurements expressed in weight percentage.
[c] speciation of the nitrogen according to the deconvolution of high-resolution N 1s core-level XPS spectra.

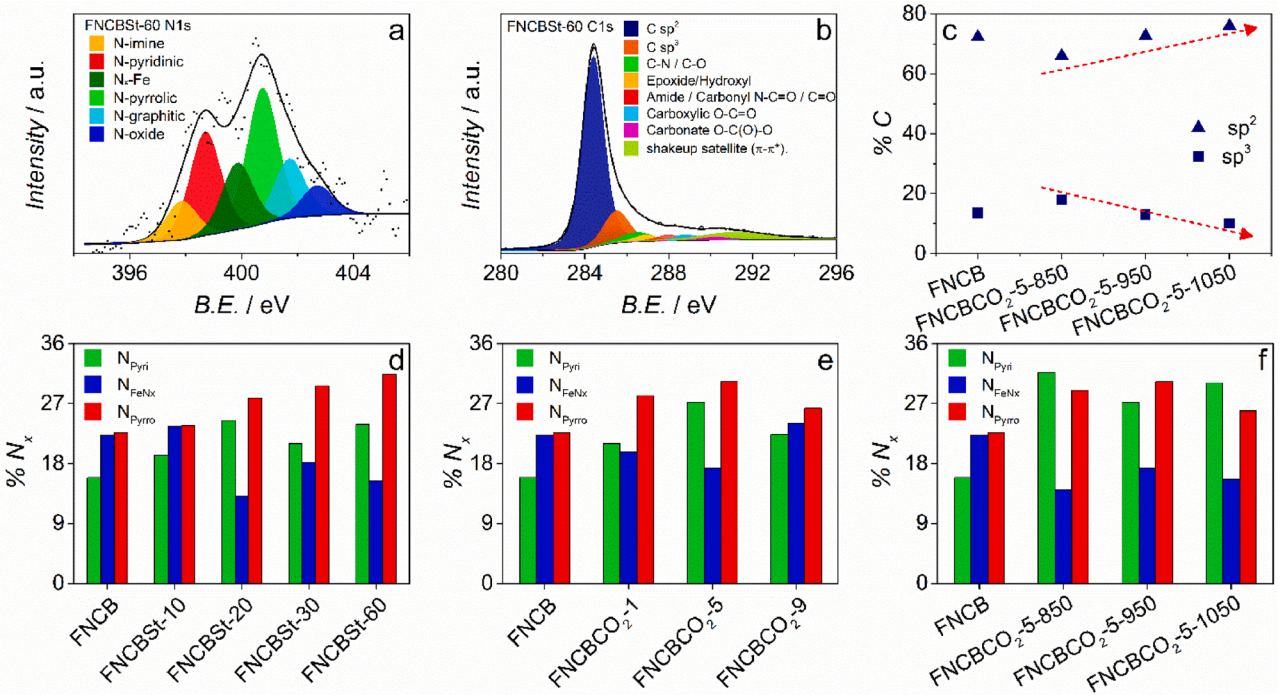

Fig. 3. a–e) TEM images of steam treated samples and f-j) TEM images of CO_2 treated ones.

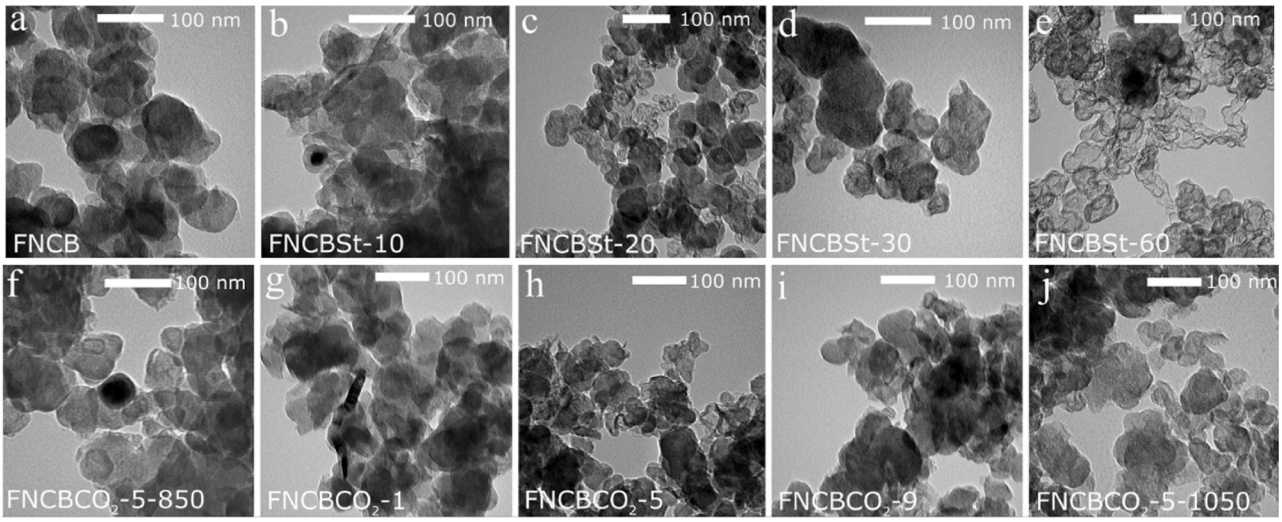

Fig. 4. High-resolution core-level XPS spectra of N 1s (a) and C 1s (b) regions and deconvolution into single chemical components, c) sp^2 and sp^3 content variation in CO_2 treated catalysts as function of temperature, d-f) nitrogen functional groups speciation derived from the deconvolution of the N 1s spectra (data resumed in Table 2).

low. Regarding this last aspect other considerations are done later when showing the electrocatalytic results.

The C 1s peak was also examined (Fig. 4b) to evaluate the sp^2/sp^3 ratio and the superficial graphitization degree. The main carbon components at BE between 284.2–284.4 eV is attributed to C-sp^2. At higher BE (285.4 eV), the peak represents the sp^3 C—C bond. There is also a substantial amount of carbon bound to nitrogen or/and to oxygen: peaks at BEs higher than 286.4 eV are due to carbon species bound to oxygen (C═O, O—C═O, O—C(O)—O) or oxygen and nitrogen (C—N═O, N—C═O). The peak at 291.1 eV is due to shakeup satellite (π-π*). [77–80] No evident changes have been observed from the C 1s high-resolution core-level XPS spectra of different samples activated in steam or CO_2, but a slight increment of sp^2 accompanied by a decrement of sp^3 is clearly visible (Fig. 4c) when the CBs were activated in CO_2 at different temperatures. All deconvolution data are reported in Tables S3 and S4.

3.3. Electrochemical characterization of Fe-N-C catalysts

In Fig. S5a,c, we report a representative example of the voltammetric behavior of FCBSt-30 and FCBCO$_2$-5 in Ar-saturated electrolyte, respectively. The other catalysts show very similar behavior. In all cases, the voltammetric background shows a couple of peaks between 0.5 V ad 0.7 V_{RHE}, which could be attributed to the reversible Fe^{3+}/Fe^{2+} and/or to a quinone/hydroquinone redox couples [13,81,82]. The samples obtained from activated CBs are also characterized by a higher capacitive current with respect to the pristine one, ascribable to the increased active surface area. In oxygen-saturated electrolyte, a very intense and

narrow peak appears at around 0.75 V_{RHE} (scan rate at 5 mV s^{-1}) which is not present in the background and is assigned to the ORR process (Fig. S5b,d). The peak potential shifts, as expected, with the variation of the scan rate, pointing out the irreversibility of the ORR reaction. Fe-N-C catalysts derived from steam activated CBs were further characterized by RRDE measurement (Fig. 5a). It clearly appears that the $E_{1/2}$ shifts to more positive value passing from FNCB to FNCBSt-60, while there is a diminution of the limiting current (j_L). The first effect can be attributed to an increase of the site density or simply an increase of the accessible sites, that allows ORR at lower overpotential. If we rely on the fact that passing from FNCB to FNCBSt-60, pyridinic and pyrrolic functional groups increase as pointed out by XPS analysis, the ORR mechanism probably follows a 2 × 2 e- pathway. This would explain also why the limiting current density is lower with respect to that expected for a 4e- pathway, and this is even more evident for the activated Fe-N-Cs. Such a difference could be related to the relatively higher loadings used for the RRDE analysis (0.6 mg cm^{-2}) resulting in a thicker catalyst layer which might hinder the H_2O_2 release. Fig. S6a reports the voltammetric behavior of FNCBCO_2-5, for different catalysts loading. It is evident the increase in capacitive current with the catalyst loading when CV are recorded in Ar purged electrolyte, while in oxygen saturated electrolyte E_p (peak potential) shifts to more positive potential and I_p (peak current) increases in module increasing the catalysts loading. From RRDE measurements, the quantity of hydrogen peroxide produced (Fig. 6Sb,c) are proportional to the loading meaning that the reduction pathway is not a pure 4e- and for higher loading some hydrogen peroxide is trapped in the material and could be further reduced to water [83]. Therefore, when a highly porous carbon is used, H_2O_2 is not further reduced to H_2O, but it is released from the electrode layer.

The histograms in Fig. 5b show two other important parameters for evaluating the ORR performance, namely kinetic current j_k and $E_{1/2}$ half-wave potential. The latter increases from 0.6 V_{RHE} to 0.654 V_{RHE} and j_k from 0.16 to 0.50 A g^{-1} (3 times higher) passing from the FNCB to the activated FNCBSt-60. Fig. 5c shows that the Tafel slope (around −100 mV dec^{-1}) does not significantly change within this set of materials and the right-shift is caused by the increment of kinetic current. Fig. 5d shows that the number of transferred electron and the quantity of hydrogen peroxide is similar for all the samples, around 3.90 and 5% at 0 V_{RHE}, respectively. The explanation of this improvement in activity must be searched in variation of morphology and chemistry of the samples. As reported in Fig. 5e and f, the almost linear correlation between both $E_{1/2}$ as well as j_k with the microporous surface (that grows linearly with treatment time as reported in Fig. 1) is rather clear. In the first instance, this should be attributed to a higher percentage of the sole Fe-N_x (not necessarily the density per unit of area) that are preferentially formed in the micropores, but from our XPS analysis this correlation is not straightforward at all.

If we rely on the XPS deconvolution, the reported improvement is only explainable by considering the overall increase of the pyridinic, pyrrolic and Fe-N_x centers. All the sites are able to catalyze the ORR to water via either the $4e^-$ pathway or the 2 × 2 electron pathway. In the latter case, reducing hydrogen peroxide before leaving the catalyst layer. In other word, the highest surface area, and in particular the higher micropore surface area, brings a preferential nitrogen functionalization to create C—N (pyridinic, pyrrolic) and Fe-N_x instead of graphitic and iminic groups, so the improvement in activity is related to a higher percentage content of groups that effectively catalyze ORR (Fig. 5g and h). An alternative explanation could be that indeed the content of Fe-N_x sites grows with micropores content but the XPS deconvolution is not enough sensitive to appreciate such difference because of the low N content and the very narrow BE range of the different species, resulting in a misinterpretation of pyridinic or pyrrolic nitrogen contribution with respect to Fe-N_x [26,84].

The evolution of the electrochemical behavior and catalytic activity versus ORR is similar also for the Fe-N-C catalysts prepared from CO_2 activated carbon (Fig. 6). The LSV recorded from CB samples, treated at different CO_2 exposure times, exhibit a well-defined plateau, with the sole exclusion of FNCBCO_2-9. It is evident that $E_{1/2}$ becomes more positive passing from FNCB to FNCBCO_2-5 (Fig. 6a), so that it results even more positive than the steam activated samples. This is not simple to explain because no evident differences emerge from the N_2 adsorption isotherms or from Raman analysis (see section 3.1). However, it is possible that CO_2 treatment leads to a wider network of interconnected pores due to the required longer treatment time (not clearly discriminable from physisorption analysis that is an average measure), which allows a better diffusion of reactants and products toward active sites. Similarly, the effect of temperature in CO_2 treatment leads to better catalytic performances with the exclusion of FNCBCO_2-5-1050. The diminution of activity observed for both FNCBCO_2-9 and FNCBCO_2-5-1050, which however showed the highest surface area among their respective sets (see Table 1), is not easy to understand considering also that for steam treatment this was not observed. Our presumption is that a too long exposure or too high temperature could promote some porogenic effect of phenanthroline that block interconnected pores and hindered the diffusion. To evaluate this possibility, a very short steam treatment (equal as previously described) has been done on FNCBCO_2-5-1050 showing unfortunately a completely loss of activity (Fig. S7), where the elemental analysis confirmed the complete loss of nitrogen

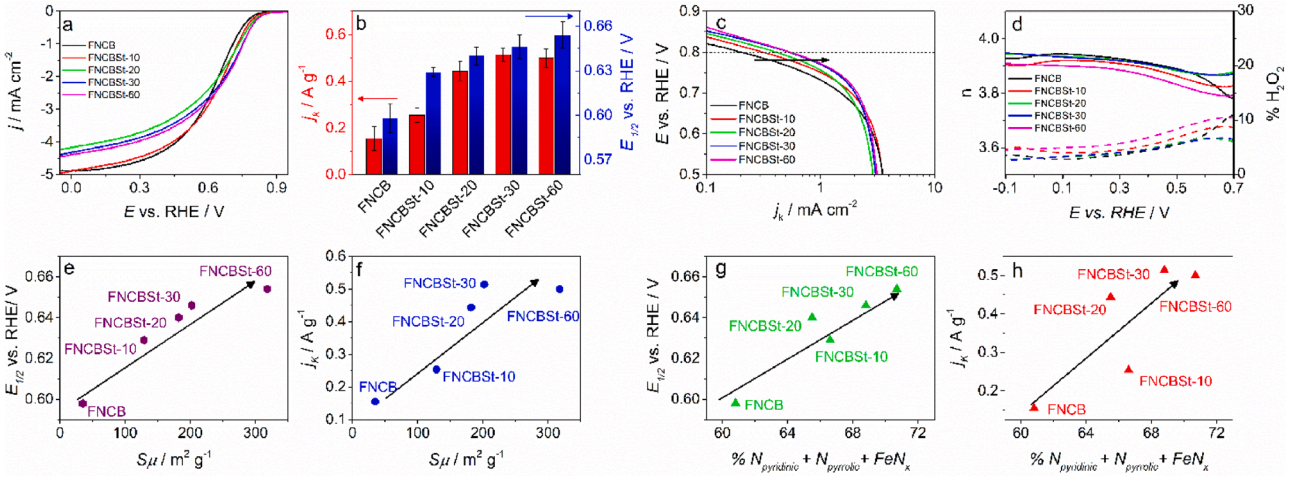

Fig. 5. a) LSV recorded in oxygen-saturated electrolyte. The scan rate was 2 mV s^{-1} and rotation speed was 1600 rpm. b) kinetic current and half-wave potential for FNCBSt-X, c) Tafel plot and d) transferred electron number and hydrogen peroxide yield derived from RRDE measurements for FNCBSt-X; e) $E_{1/2}$ and f) j_k correlations with surface area of micropores; g) $E_{1/2}$ and h) j_k correlation with pyridinic, pyrrolic and Fe-N_x group percentage (see Table 2).

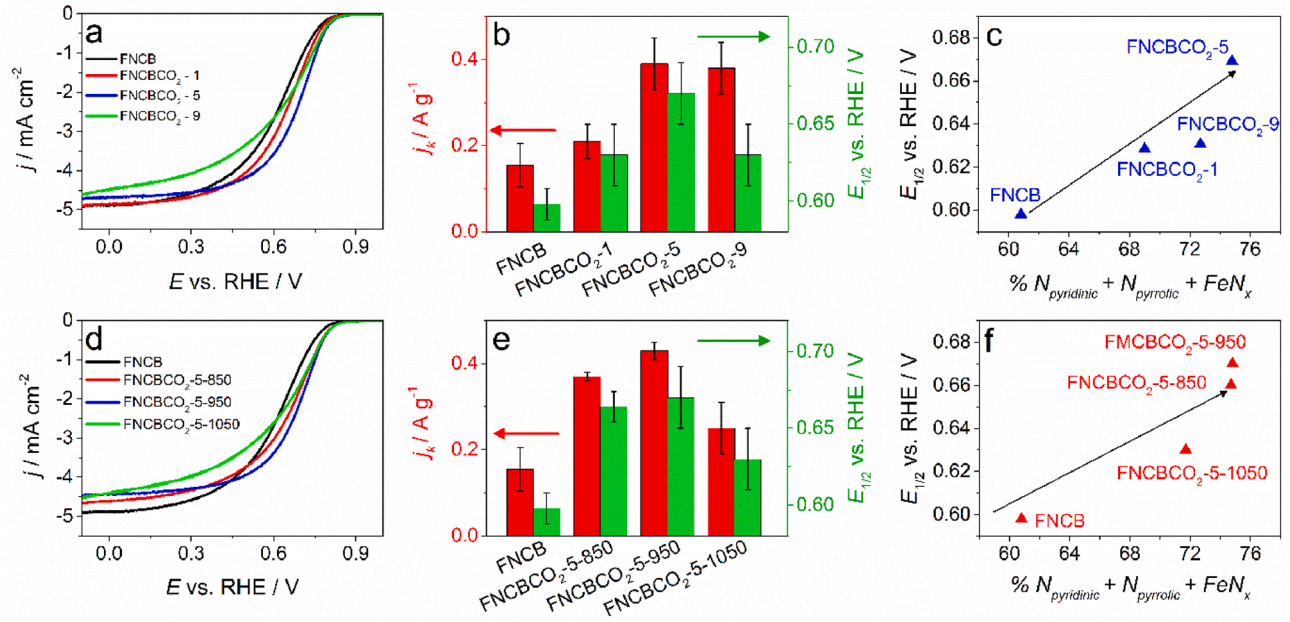

Fig. 6. LSV recorded in oxygen-saturated electrolyte for CO_2 series of samples for time effect (a) and temperature effect (d). The scan rate was 2 mV s^{-1} and rotation speed was 1600 rpm. kinetic current and half-wave potential for (b) FNCBCO$_2$-X and (e) FNCBCO$_2$-5-Y; $E_{1/2}$ correlations with with pyridinic, pyrrolic and Fe-N$_x$ group percentage for (c) FNCBCO$_2$-X and (f) FNCBCO$_2$-5-Y; (see Table 2).

(Table S5). This result is anyway interesting because it could indicate that the nitrogen functionalization is almost restricted on the surface. Also for the CO_2 activated Fe-N-C catalysts, a correlation between $E_{1/2}$ or j_k with the nitrogen content is evident (Fig. 6c and f), but it was not possible to discriminate whether this would be due to the increasing of the sole Fe-N$_x$ sites with respect to the pyrrolic and pyridinic sites or *vice versa*, as XPS analysis indicated. Among other common techniques used for characterizing Fe-N-C, ^{57}Fe Mössbauer Spectroscopy is surely a powerful tool to characterize Fe-N$_x$ bearing materials. However, as this technique is sensitive to ^{57}Fe, which is ≈2% of natural iron, this aspect excludes its application to materials with a low load of natural Fe (usually lower than 1–2 % in weight, expressed as Fe_2O_3) as in the present case and also require to be prepared in larger amount.

Another option to quantify the number of Fe-N$_x$ sites relies on the electrochemical nitrite stripping developed by Malko et al. [36,85,86]. This method is based on the selective interaction of Fe-N$_x$ sites with

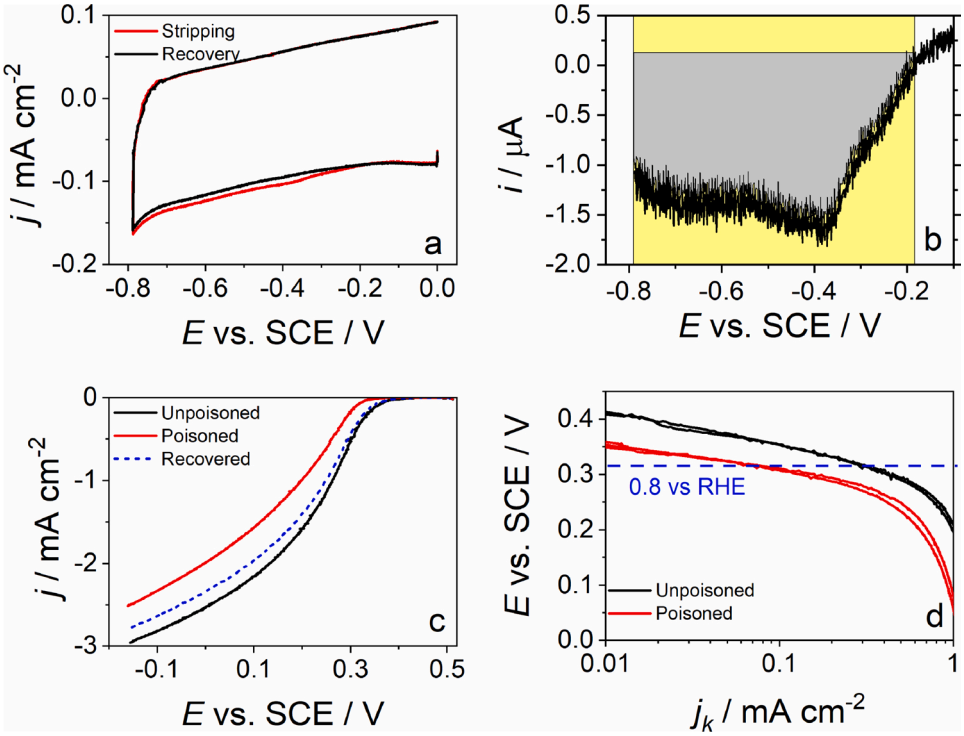

Fig. 7. a) nitrite stripping and recovered CVs of FNCBCO$_2$-5 recorded in Ar-saturated electrolyte at 10 mV s^{-1}, b) magnification of the stripping area integrated for the site density determination, c) LSV recorded before, during and after poisoning at 1600 rpm and 5 mV s^{-1} in O_2-saturated electrolyte, and d) Tafel plots for the poisoned and recovered catalyst.

probe molecule NO_2^-, NO or NH_2OH [see reference above] which reversibly binds to the Fe center as nitrosyl at mildly acidic pH value of 5.2. When the catalyst layer is poisoned, there is an excess of cathodic charge, Q_{strip}, which can be related to the gravimetric site density according to the formula:

$$\mathrm{MSD}\left[\text{mol sites g}^{-1}\right] = \frac{Q_{strip}\left[\text{C g}^{-1}\right]}{n_{strip}F\left[\text{C mol}^{-1}\right]} \quad (8)$$

where n_{strip} is the number of electrons associated with the reduction of one adsorbed nitrosyl per site to NH_3.

What we expected to observe was an increment in sites density due to the increment of micro and mesopores and probably an increment in TOF which would justify the increment in activity. The activity in terms of kinetic current is given by the expression:

$$j_K = F{\cdot}TOF{\cdot}MSD \quad (9)$$

where F is the Faraday constant, TOF is the turnover frequency of Fe-N_x sites and MSD the gravimetric active sites density. So, an active catalyst could be obtained either from a high turnover frequency or a high accessibility to sites.

An example of the obtained electrochemical curves is reported in Fig. 7, while the full collection of data are reported in Table 3. A clear reductive current is evident in Fig. 7a due to nitrite stripping, as highlighted by the difference between the two curves (Fig. 7b). The diminution in activity at 0.8 V_{RHE} (0.309 vs. SCE) is clear from LSV and Tafel plots (Fig. 7c and d). The recovered LSV, i.e. the LSV recorded after the NO stripping, shows that most of the activity is recovered but there is a diminution in current at higher overpotential. This could be caused by some sites that are permanently poisoned or more probable due to a time-dependent catalyst degradation. It is worth noting that the shape of LSV are stretched compared with LSV in Fig. 5 probably due to the effect of electrolyte or lower catalyst loading (0.2 mg cm^{-2}) used for the nitrite stripping versus 0.6 mg cm^{-2} employed for all the other electrochemical measurements.

It is interesting to observe that according to NO-stripping findings, the site density increases almost linearly both with respect to micropore surface area and volume (but also for mesopores). This outcome is in disagreement with the XPS findings. Therefore, increasing the activation treatment both in terms of time and temperature favored the subsequent formation of Fe-N_x sites. A more porous network allows higher functionalization, whereas a more open structure entails a higher accessibility to sites and as a consequence, a global higher site density (Fig. 8a). Carbon dioxide treatment seems to be more effective than steam treatment in increasing the site density. As it was said before this could be caused by an interconnected pore structure which is not discriminable with the physisorption analysis. There is also a good correlation between activity, in term of kinetic current (Fig. 8b), and TOF calculated at 0.8 V_{RHE}. This time the correlation seems less dependent on the type of treatment, but again carbon dioxide leads to a higher TOF, which is probably due to a higher accessibility (easier diffusion to Fe-N_x sites). In general, these two correlations combined together are in perfect agreement with the increment of kinetic current at 0.8 V (as well as onset potential) with increasing time treatment. Finally, a map plotting TOF vs. SD is proposed in order to show that higher activity could be achieved both increasing sites density and the turnover frequency. The graph (Fig. 8c) allows to observe that the steam-activated samples show an almost linear increment crossing the isocurves of kinetic current (gray lines), that means that both SD and TOF contribute to the increasing of activity. It is interesting to observe that the percentage of "effective iron" i.e. the percentage of iron active for ORR that can be counted by nitrite poisoning with respect the total amount of iron determined by XPS increases from 2.65 in FNCB to 11.01 % in FNCBSt60 (Table 3). Malko at al. discovered that only about 4.5 % of the iron in the sample was active for ORR. [36] Therefore, it appears clear that steam treatments help in opening up the structure, allowing a better access of electrolyte to the iron sites. Therefore, it would be in principle possible to further increase the kinetic current to a certain extent just by extending the steam treatment. Clearly, this last reasoning does not consider that the subsequent functionalization with Fe-N_x sites is in any case limited by the capability of fixing Fe-N_x while not changing the textural properties.

For the CO_2 sets, it appears that the activated samples move along a single isocurve, indeed these sample are in general more active but some for a higher SD and others for higher TOFs. In fact, passing from FNCB to FNCBCO_2-5 the activity increases because TOF increases, whereas FNCBCO_2-9 moves up to higher SD value but to lower TOF. This is in accordance with the observation that micropore gets longer easier than they are widened, so that the formation of Fe-N_x can indeed increase. However, if this is not followed by a suitable increase of volume/area of mesopore, the active sites remain hardly reachable which could lead to lower TOFs. Also, CO_2 treatments allows an increase of iron active site utilization touching the 14.72 % in FNCBCO2-5 h-1050 (Table 3). Therefore, also in this case we can claim that CO_2 activation involve the formation of a more open and accessible structure where allowing better access of electrolyte to the active sites.

Fig. 8d compares the model samples prepared in this work with benchmark samples used in Primbs at al. work, which represent the state of the art Fe-N-C materials for ORR. [12] Primbs paper evaluated in depth the Fe surface site densities and TOF values and compared the same set of Fe–N–C catalysts using in situ nitrite reduction and ex situ CO cryo adsorption. It is clear that the carbon activation with CO_2 and

Table 3
Electrochemical data determined by RRDE measurements in 0.5 M H_2SO_4 and NO stripping in 0.5 M acetate buffer at pH 5.2.

	$E_{1/2}$ [a,b] V	j_K [b,c] A g^{-1}	$j_{0.8V}$ [b,c] mA cm^{-2}	n [d] –	H_2O_2 [d] %	Q_{STRIP} C g^{-1}	Δj_k [e] A g^{-1}	SD sites g^{-1}	MSD mol sites g^{-1}	TOF (0.8 V) e^- sites^{-1} s^{-1}	Fe_{eff}
FNCB	0.60 ± 0.01	0.16 ± 0.05	0.11 ± 0.01	3.88	3.9	0.94	0.14	1.17E+18	1.94E-06	0.76	2.65
FNCBSt-10	0.629 ± 0.003	0.25 ± 0.03	0.16 ± 0.03	3.91	4.6	1.21	0.33	1.51E+18	2.51E-06	1.37	3.40
FNCBSt-20	0.640 ± 0.006	0.44 ± 0.04	0.26 ± 0.04	3.94	3.0	1.72	0.78	2.14E+18	3.56E-06	2.27	4.36
FNCBSt-30	0.646 ± 0.008	0.51 ± 0.03	0.38 ± 0.11	3.94	3.0	2.45	1.03	3.06E+18	5.08E-06	2.09	5.66
FNCBSt-60	0.654 ± 0.009	0.50 ± 0.04	0.34 ± 0.07	3.90	4.8	2.61	1.30	3.26E+18	5.41E-06	2.48	11.01
FNCBCO_2-1	0.63 ± 0.02	0.21 ± 0.04	0.13 ± 0.02	3.95	2.3	1.68	1.00	2.10E+18	3.48E-06	2.98	5.36
FNCBCO_2-5	0.67 ± 0.02	0.39 ± 0.06	0.23 ± 0.05	3.99	0.7	1.91	1.49	2.38E+18	3.96E-06	3.90	8.08
FNCBCO_2-9	0.63 ± 0.02	0.38 ± 0.06	0.24 ± 0.04	3.93	3.3	3.35	1.37	4.18E+18	6.95E-06	2.04	6.16
FNCBCO_2-5-850	0.66 ± 0.01	0.37 ± 0.01	0.1 ± 0.05	3.93	3.6	1.31	1.00	1.63E+18	2.71E-06	3.84	1.78
FNCBCO_2-5-950	0.67 ± 0.02	0.43 ± 0.02	0.23 ± 0.05	3.99	0.7	1.91	1.49	2.38E+18	3.96E-06	3.90	8.08
FNCBCO_2-5-1050	0.63 ± 0.02	0.25 ± 0.06	0.20 ± 0.05	3.90	5.0	2.32	1.33	2.89E+18	4.80E-06	2.88	14.72

[a] vs. RHE.
[b] Error are reported as standard deviation of multiple measurements.
[c] at 0.8 V vs. RHE.
[d] at 0.0 V vs. RHE.
[e] difference in kinetic current before and after poisoning (0.5 M acetate buffer at pH 5.2) at 0.309 V vs. SCE (0.8 vs RHE).

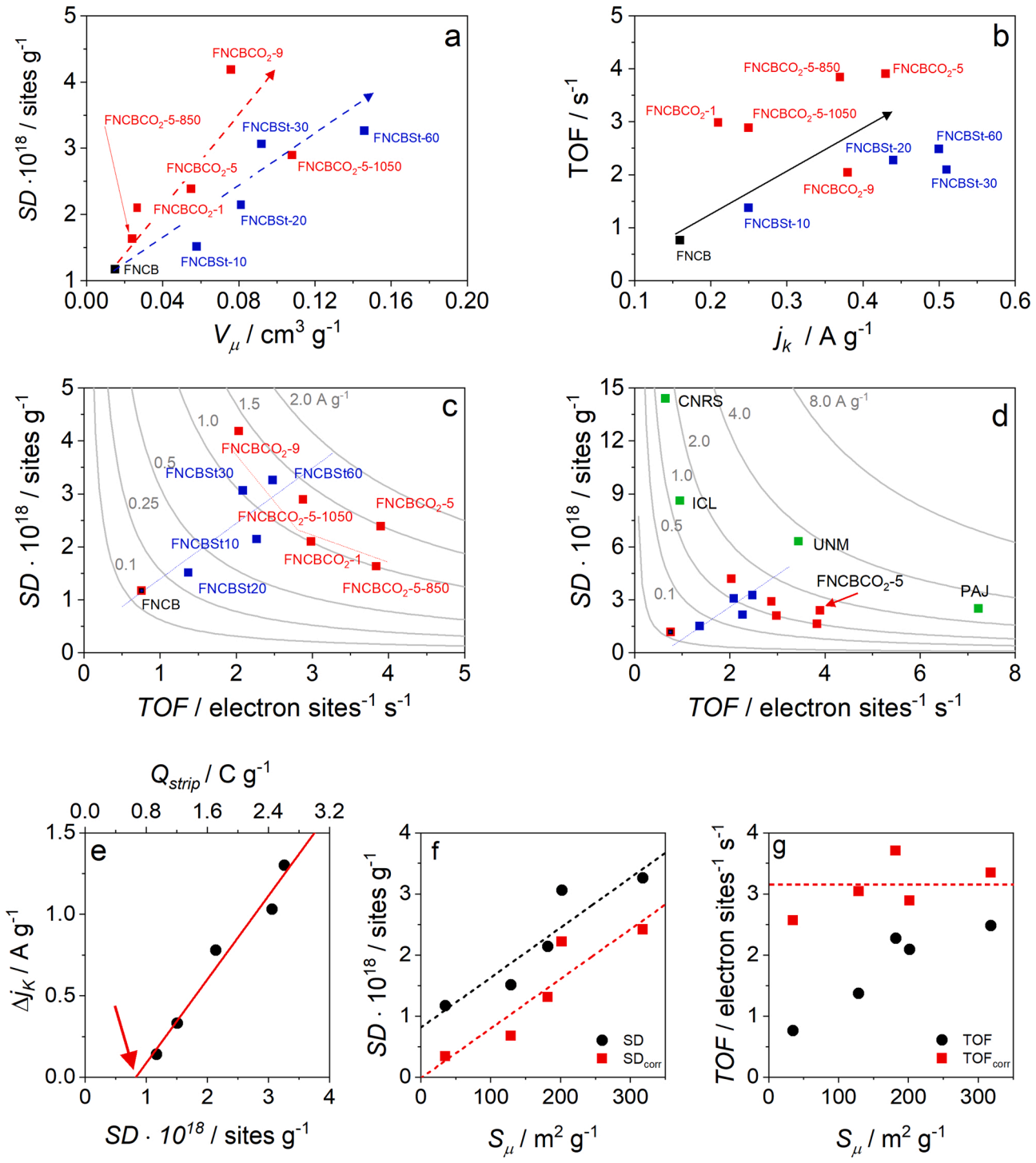

Fig. 8. a) SD correlation with microporous volume; b) correlation between TOF and kinetic current at 0.8 V vs RHE; c) Activity map of all catalysts, in blue the steam sets and in red the CO_2 sets, grey lines represent the iso-current line which are hyperbole according to Eq. (9) while blue dotted line are intended for guiding the eye from low to high catalytic activity; d) comparison with benchmark catalysts described by Primbs et al. e) SD vs. difference in kinetic current due to poisoning, f) SD and b) TOF before and after correction against microporous surface area.

steam leads to a more open structure, which in the end resemble preferentially to the behavior of UNM or Pajarito powder(PAJ), i.e. the catalysts with specific textural properties induced by the hard template synthesis. This apparently means that increasing the micro and mesopore surface and volume helps preferentially the enhancement of TOF than the SD. To increase the SD as in CNRS and ICL catalysts, it is necessary to change the type of Fe-N_x precursor that must be able to efficiently pin the active sites avoiding the clogging of micro and mesopores.

Regarding the increase of TOF we can make more insightful consideration by considering the sole steam sets. If we plot the change in kinetic activity with stripping charge (or site density), we see that there is good straight-line dependence, but the intercept is not zero (Fig. 8e). This hold strongly with steam sets material although this effect is not so strong for the CO_2 treated material possibly because of the interaction of NO_2 with other iron species such as Fe_2O_3 even if Fe_2O_3 was not detected

by XRD or XPS analysis. This appears to suggest that there are a given number of sites that are "inactive" for the ORR, or alternatively we overestimate the stripping charge by a constant amount for all catalysts (that amount is 0.667 C g^{-1} based on the intercept) and we should ignore those sites – i.e. we should subtract the "inactive" sites from the total sites:

$$Q_{strip,corr} = Q_{strip} - 0.667\ C\ g^{-1}$$

If we correct the site densities and TOF (Table S6) and we plot against the microporous surface area (valid also for the volume) which is one of the main parameters that differentiate these materials, we see that a new description is possible, the increment in activity is mainly due to SD increment and the TOF is oscillating around an average value of 3.11 ± 0.39 electron $sites^{-1}$ s^{-1} (Fig. 8f,g). Looking at the slope (8.11 $\cdot 10^{15}$ sites m^{-2}) of red fitting in Fig. 8b, it is possible to estimate the average distance of sites, using the expression:

$$d = \frac{1}{\sqrt{slope}}$$

Which gives about 11 nm of average distance between two sites. The same effect, as said, is not evident on CO_2 set, we do not have particular clue on why this append, but it could be the case of an underestimation of sites or some difference on sites, but in absence of concrete evidence we do not do speculation.

Long lasting chronoamperometries (9 h) experiments were carried out on three representative catalysts, i.e FNCB, FNCBSt60 and FNCBCO$_2$-5 for gauging any variation in perforce due to degradation issues. Chronoamperometry was performed in O_2-saturated 0.5 M H_2SO_4 electrolyte at a rotation speed of 200 rpm and controlled temperature of 25 °C. Control LSVs were recorded at the beginning of each experiment and then every 3 h (Fig. 9). The aim was to understand if there was any evident change in stability related to the different treatment done on the carbon.

After 9 h at a constant potential of 0.15 V vs. RHE a current drop was observed at all the tested materials in the range 8–20 %, FNCBSt60 being apparently the less affected by performance loss. Furthermore, we observe a variation of the half-wave potential for recorded LSV, that decreases for each sample but to a different extent i.e. 8 % ($\Delta E_{1/2}$ = 39 mV), 3% ($\Delta E_{1/2}$ = 21 mV) and 12 % ($\Delta E_{1/2}$ = 80 mV) for FNCB, FNCBSt60 and FNCBCO$_2$-5, respectively (Fig. 9d–f). If we compare the three samples it is possible to observed that FNCBSt60 seems slightly more stable than the other two, but we cannot give any further consideration. More in general is not easy to compare result with other works because different potential, rotation speed, loading and electrolyte condition are used, but we could anyway point out that a decreasing of 20 % after 9 h are in line with other Fe-N-C catalysts [87]. In conclusion we can assert that the steam or CO_2 thermal treatments does not bring further severe stability issues with respect to the pristine catalyst material.

4. Conclusion

In this work, the effect of activation of CB, namely a controlled evolution of micro and mesopores content was carried out in order to study the influence of carbon support on site formation and activity in Fe-N-C catalysts prepared by thermal treatment of activated carbons with $Fe(Phen)_3Cl_2$. All the activated supports give higher activity if compared with the pristine one, where the steam treatment allows to obtain a faster evolution of pore and a good improvement in activity (three time higher kinetic current at 0.8 V). It was established that standard XPS analysis leads to not fully precise interpretation of N 1s spectrum since it is difficult to single out the contribution of the Fe-N_x components with respect to the pyridinic and pyrrolic one especially when the nitrogen content is low (< 1). It was also demonstrated that nitrite stripping allowed to characterize the electrochemical accessible site density of Fe-N_x centres showing that the improvement in activity is both caused by an increment in site density and turnover frequency. The percentage of iron active for ORR that can be counted by nitrite poisoning with respect the total amount of iron determined by XPS increases from 2.65 in FNCB to 11.01 % and to 14.74 in FNCBSt60 and FNCBCO2-5-1050, respectively, confirming that steam and CO_2 treatments help in opening up the structure, allowing deposition of more sites and a better access to sites. This is in good agreement with evolution of micro and mesopore in the support indicating the importance pore structure in carbon precursor, in particular the role of micro and meso pore is important either in site formation and/or site accessibility. It is however important to stress that microporosity should be accompanied with adequate mesoporosity to prevent flooding and capillary

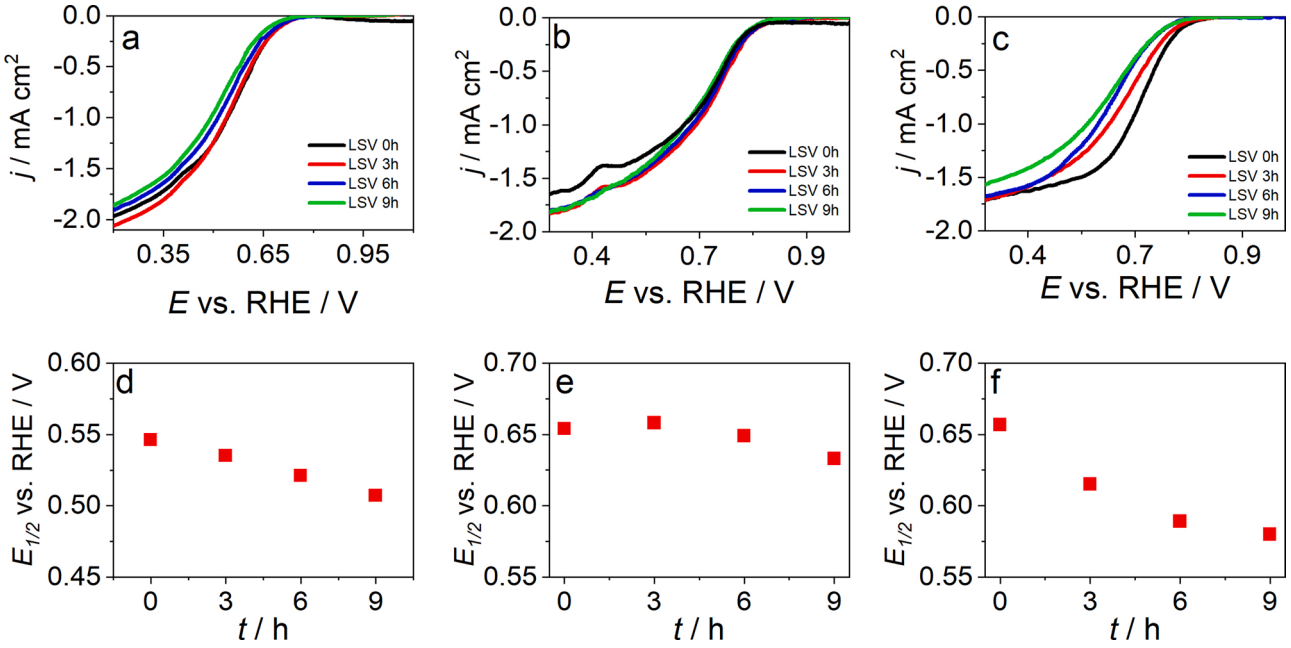

Fig. 9. (a–c) LSV and (d-f) half wave potential variation recorded every 3 h during the chronoamperometry stability test at RDE (ω =200 rpm) in O_2-saturated 0.5 M H_2SO_4 electrolyte at (a,d) FNCB, (b,e) FNCBSt60 and (c,f) FNCBCO$_2$-5.

condensation effects into micropores when passing to test the electrode material in a full MEA.

CRediT authorship contribution statement

Marco Mazzucato: Data curation, Writing - original draft. **Giorgia Daniel:** Data curation. **Asad Mehmood:** Data curation. **Tomasz Kosmala:** Data curation. **Gaetano Granozzi:** Paper revision. **Anthony Kucernak:** Data curation. **Christian Durante:** Conceptualization, Data curation, Writing - review & editing.

Declaration of Competing Interest

The authors declare that they have no known competing financial interests or personal relationships that could have appeared to influence the work reported in this paper.

Acknowledgments

The research leading to these results has received funding from the Fuel Cells and Hydrogen 2 Joint Undertaking under grant agreement No 779366, CRESCENDO. This Joint Undertaking receives support from the European Union's Horizon 2020 research and innovation programme, Hydrogen Europe and Hydrogen Europe Research.

Appendix A. Supplementary data

Supplementary data associated with this article can be found, in the online version, at https://doi.org/10.1016/j.apcatb.2021.120068.

References

[1] M. Shao, Q. Chang, J.-P. Dodelet, R. Chenitz, Recent advances in electrocatalysts for oxygen reduction reaction, Chem. Rev. 116 (2016) 3594–3657.
[2] O.T. Holton, J.W. Stevenson, The role of platinum in proton exchange membrane fuel cells, Platin. Met. Rev. (October) (2013) 259–271.
[3] Y. Zhang, X. Du, M. Salman, Battery state estimation with a self-evolving electrochemical ageing model, Int. J. Electr. Power Energy Syst. 85 (2017) 178–189.
[4] R. Brandiele, V. Amendola, A. Guadagnini, G.A. Rizzi, D. Badocco, P. Pastore, A. A. Isse, C. Durante, A. Gennaro, Facile synthesis of Pd_3Y alloy nanoparticles for electrocatalysis of the oxygen reduction reaction, Electrochim. Acta 320 (2019) 134563–134572.
[5] R. Brandiele, A. Guadagnini, L. Girardi, G. Dražić, M.C. Dalconi, G.A. Rizzi, V. Amendola, C. Durante, Climbing the oxygen reduction reaction volcano plot with laser ablation synthesis of Pt x Y nanoalloys, Catal. Sci. Technol. 10 (14) (2020) 4503–4508.
[6] R. Brandiele, C. Durante, E. Grądzka, G.A. Rizzi, J. Zheng, D. Badocco, P. Centomo, P. Pastore, G. Granozzi, A. Gennaro, One step forward to a scalable synthesis of platinum–Yttrium alloy nanoparticles on mesoporous carbon for the oxygen reduction reaction, J. Mater. Chem. A 4 (31) (2016) 12232–12240.
[7] Y.-J. Wang, W. Long, L. Wang, R. Yuan, A. Ignaszak, B. Fang, D.P. Wilkinson, Unlocking the door to highly active ORR catalysts for PEMFC applications: polyhedron-engineered Pt-Based nanocrystals, Energy Environ. Sci. 11 (2) (2018) 258–275.
[8] X. Huang, Z. Zhao, L. Cao, Y. Chen, E. Zhu, Z. Lin, M. Li, A. Yan, A. Zettl, Y. M. Wang, X. Duan, T. Mueller, Y. Huang, High-performance transition metal-doped Pt3Ni octahedra for oxygen reduction reaction, Science 348 (6240) (2015) 1230–1234.
[9] V. Perazzolo, R. Brandiele, C. Durante, M. Zerbetto, V. Causin, G.A. Rizzi, I. Cerri, G. Granozzi, A. Gennaro, Density functional theory (DFT) and experimental evidences of metal–support interaction in platinum nanoparticles supported on nitrogen- and sulfur-doped mesoporous carbons: synthesis, activity, and stability, ACS Catal. 8 (2) (2018) 1122–1137.
[10] R. Brandiele, C. Durante, M. Zerbetto, N. Vicentini, T. Kosmala, D. Badocco, P. Pastore, G.A. Rizzi, A.A. Isse, A. Gennaro, Probing the correlation between Pt-support interaction and oxygen reduction reaction activity in mesoporous carbon materials modified with Pt-N active sites, Electrochim. Acta 277 (2018) 287–300.
[11] R. Brandiele, M. Zerbetto, M.C. Dalconi, G.A. Rizzi, A.A. Isse, C. Durante, A. Gennaro, Mesoporous carbon with different density of thiophenic-like functional groups and their effect on oxygen reduction, ChemSusChem 12 (18) (2019) 4229–4239.
[12] M. Primbs, Y. Sun, A. Roy, D. Malko, A. Mehmood, M.-T. Sougrati, P.-Y. Blanchard, G. Granozzi, T. Kosmala, G. Daniel, P. Atanassov, J. Sharman, C. Durante, A. Kucernak, D. Jones, F. Jaouen, P. Strasser, Establishing reactivity descriptors for platinum group metal (PGM)-Free Fe–N–C catalysts for PEM fuel cells, Energy Environ. Sci. 13 (8) (2020) 2480–2500.
[13] F. Jaouen, J. Herranz, M. Lefèvre, J.-P. Dodelet, U.I. Kramm, I. Herrmann, P. Bogdanoff, J. Maruyama, T. Nagaoka, A. Garsuch, J.R. Dahn, T. Olson, S. Pylypenko, P. Atanassov, E.A. Ustinov, Cross-laboratory experimental study of non-noble-metal electrocatalysts for the oxygen reduction reaction, ACS Appl. Mater. Interfaces 1 (8) (2009) 1623–1639.
[14] F. Xiao, G.-L. Xu, C.-J. Sun, M. Xu, W. Wen, Q. Wang, M. Gu, S. Zhu, Y. Li, Z. Wei, X. Pan, J. Wang, K. Amine, M. Shao, Nitrogen-coordinated single Iron atom catalysts derived from metal organic frameworks for oxygen reduction reaction, Nano Energy 61 (2019) 60–68.
[15] I. Matanovic, K. Artyushkova, P. Atanassov, Understanding PGM-Free catalysts by linking density functional theory calculations and structural analysis: perspectives and challenges, Curr. Opin. Electrochem. 9 (2018) 137–144.
[16] G. Daniel, T. Kosmala, M.C. Dalconi, L. Nodari, D. Badocco, P. Pastore, A. Lorenzetti, G. Granozzi, C. Durante, Upcycling of polyurethane into iron-nitrogen-carbon electrocatalysts active for oxygen reduction reaction, Electrochim. Acta 362 (2020), 137200.
[17] G. Daniel, E. Foltran, R. Brandiele, L. Nodari, R. Pilot, E. Menna, G.A. Rizzi, A. A. Isse, C. Durante, A. Gennaro, Platinum-free electrocatalysts for oxygen reduction reaction: Fe-Nx modified mesoporous carbon prepared from biosources, J. Power Sources 402 (2018) 434–446.
[18] X. Ge, A. Sumboja, D. Wuu, T. An, B. Li, F.W.T. Goh, T.S.A. Hor, Y. Zong, Z. Liu, Oxygen reduction in alkaline media: from mechanisms to recent advances of catalysts, ACS Catal. 5 (8) (2015) 4643–4667.
[19] U. Martinez, S. Komini Babu, E.F. Holby, P. Zelenay, Durability challenges and perspective in the development of PGM-Free electrocatalysts for the oxygen reduction reaction, Curr. Opin. Electrochem. 9 (2018) 224–232.
[20] T. Mineva, I. Matanovic, P. Atanassov, M.-T. Sougrati, L. Stievano, M. Clémancey, A. Kochem, J.-M. Latour, F. Jaouen, Understanding active sites in pyrolyzed Fe–N–C catalysts for fuel cell cathodes by bridging density functional theory calculations and 57 Fe Mössbauer spectroscopy, ACS Catal. 9 (10) (2019) 9359–9371.
[21] M.W. Chung, G. Chon, H. Kim, F. Jaouen, C.H. Choi, Electrochemical evidence for two sub-families of FeN_xC_y moieties with concentration-dependent cyanide poisoning, ChemElectroChem 5 (14) (2018) 1880–1885.
[22] A. Zitolo, V. Goellner, V. Armel, M.-T. Sougrati, T. Mineva, L. Stievano, E. Fonda, F. Jaouen, Identification of catalytic sites for oxygen reduction in Iron- and nitrogen-doped graphene materials, Nat. Mater. 14 (9) (2015) 937–942.
[23] Q. Jia, N. Ramaswamy, U. Tylus, K. Strickland, J. Li, A. Serov, K. Artyushkova, P. Atanassov, J. Anibal, C. Gumeci, S.C. Barton, M.-T. Sougrati, F. Jaouen, B. Halevi, S. Mukerjee, Spectroscopic insights into the nature of active sites in Iron–Nitrogen–Carbon electrocatalysts for oxygen reduction in acid, Nano Energy 29 (2016) 65–82.
[24] Y.J. Sa, J.H. Kim, S.H. Joo, Recent progress in the identification of active sites in pyrolyzed Fe−N/C catalysts and insights into their role in oxygen reduction reaction, J. Electrochem. Sci. Technol. 8 (3) (2017) 169–182.
[25] S. Kattel, P. Atanassov, B. Kiefer, A density functional theory study of oxygen reduction reaction on Non-PGM Fe–Nx–C electrocatalysts, Phys. Chem. Chem. Phys. 16 (27) (2014) 13800.
[26] K. Artyushkova, I. Matanovic, B. Halevi, P. Atanassov, Oxygen binding to active sites of Fe–N–C ORR electrocatalysts observed by ambient-pressure XPS, J. Phys. Chem. C 121 (5) (2017) 2836–2843.
[27] S. Kattel, G. Wang, A density functional theory study of oxygen reduction reaction on Me-N 4 (Me = Fe, Co, or Ni) clusters between graphitic pores, J. Mater. Chem. A 1 (36) (2013) 10790–10797.
[28] U. Tylus, Q. Jia, K. Strickland, N. Ramaswamy, A. Serov, P. Atanassov, S. Mukerjee, Elucidating oxygen reduction active sites in Pyrolyzed Metal–Nitrogen coordinated non-precious-metal electrocatalyst systems, J. Phys. Chem. C 118 (17) (2014) 8999–9008.
[29] K. Artyushkova, A. Serov, S. Rojas-Carbonell, P. Atanassov, Chemistry of multitudinous active sites for oxygen reduction reaction in transition metal–nitrogen–carbon electrocatalysts, J. Phys. Chem. C 119 (46) (2015) 25917–25928.
[30] Y.N. Sun, M.L. Zhang, L. Zhao, Z.Y. Sui, Z.Y. Sun, B.H.A.N. Han, P dual-doped carbon with high porosity as an advanced metal-free oxygen reduction catalyst, Adv. Mater. Interfaces 6 (14) (2019) 1–9.
[31] B. Zheng, J. Wang, F. Bin Wang, X.H. Xia, Synthesis of nitrogen doped graphene with high electrocatalytic activity toward oxygen reduction reaction, Electrochem. Commun. 28 (2013) 24–26.
[32] A. Kozhushner, N. Zion, L. Elbaz, Methods for assessment and measurement of the active site density in platinum group metal–Free oxygen reduction reaction catalysts, Curr. Opin. Electrochem. (2020) 1–10.
[33] M.S. Thorum, J.M. Hankett, A.A. Gewirth, Poisoning the oxygen reduction reaction on carbon-supported Fe and Cu electrocatalysts: evidence for metal-centered activity, J. Phys. Chem. Lett. 2 (4) (2011) 295–298.
[34] J.L. Kneebone, S.L. Daifuku, J.A. Kehl, G. Wu, H.T. Chung, M.Y. Hu, E.E. Alp, K. L. More, P. Zelenay, E.F. Holby, M.L. Neidig, A combined probe-molecule, Mössbauer, nuclear resonance vibrational spectroscopy, and density functional theory approach for evaluation of potential iron active sites in an oxygen reduction reaction catalyst, J. Phys. Chem. C 121 (30) (2017) 16283–16290.
[35] N.R. Sahraie, U.I. Kramm, J. Steinberg, Y. Zhang, A. Thomas, T. Reier, J. P. Paraknowitsch, P. Strasser, Quantifying the density and utilization of active sites in non-precious metal oxygen electroreduction catalysts, Nat. Commun. 6 (1) (2015) 1–9.

[36] D. Malko, A. Kucernak, T. Lopes, In situ electrochemical quantification of active sites in Fe–N/C non-precious metal catalysts, Nat. Commun. 7 (2016) 13285–13292.
[37] V. Nallathambi, N. Leonard, R. Kothandaraman, S.C. Barton, Nitrogen precursor effects in iron-nitrogen-carbon oxygen reduction catalysts, Electrochem. Solid-State Lett. 14 (6) (2011) B55.
[38] R. Jäger, P.E. Kasatkin, E. Härk, P. Teppor, T. Romann, R. Härmas, I. Tallo, U. Mäeorg, U. Joost, P. Paiste, K. Kirsimäe, E. Lust, The effect of N precursors in Fe-N/C type catalysts based on activated silicon carbide derived carbon for oxygen reduction activity at various PH values, J. Electroanal. Chem. 823 (2018) 593–600.
[39] C.W.B. Bezerra, L. Zhang, K. Lee, H. Liu, A.L.B. Marques, E.P. Marques, H. Wang, J. Zhang, A review of Fe-N/C and Co-N/C catalysts for the oxygen reduction reaction, Electrochim. Acta 53 (15) (2008) 4937–4951.
[40] V. Perazzolo, G. Daniel, R. Brandiele, L. Picelli, G.A. Rizzi, A.A. Isse, C. Durante, PEO-b-PS block copolymer templated mesoporous carbons: a comparative study of nitrogen and sulfur doping in the oxygen reduction reaction to hydrogen peroxide, Chem. – A Eur. J. (2020) chem.202003355.
[41] X. Wang, H. Zhang, H. Lin, S. Gupta, C. Wang, Z. Tao, H. Fu, T. Wang, J. Zheng, G. Wu, X. Li, Directly converting Fe-Doped metal-organic frameworks into highly active and stable Fe-N-C catalysts for oxygen reduction in acid, Nano Energy 25 (2016) 110–119.
[42] J. Tian, A. Morozan, M.T. Sougrati, M. Lefèvre, R. Chenitz, J.-P. Dodelet, D. Jones, F. Jaouen, Optimized synthesis of Fe/N/C cathode catalysts for PEM fuel cells: a matter of iron-ligand coordination strength, Angew. Chemie Int. Ed. 52 (27) (2013) 6867–6870.
[43] G. Wu, K.L. More, C.M. Johnston, P. Zelenay, High-performance electrocatalysts for oxygen reduction reaction derived from polyaniline, iron, and cobalt, Science 332 (2011) 443–447.
[44] U.I. Kramm, I. Herrmann-Geppert, S. Fiechter, G. Zehl, I. Zizak, I. Dorbandt, D. Schmeißer, P. Bogdanoff, Effect of iron-carbide formation on the number of active sites in Fe-N-C catalysts for the oxygen reduction reaction in acidic media, J. Mater. Chem. A 2 (8) (2014) 2663–2670.
[45] U.I. Kramm, I. Herrmann-Geppert, J. Behrends, K. Lips, S. Fiechter, P. Bogdanoff, On an easy way to prepare metal–nitrogen doped carbon with exclusive presence of MeN_4-type sites active for the ORR, J. Am. Chem. Soc. 138 (2) (2016) 635–640.
[46] X.M. Hu, H.H. Hval, E.T. Bjerglund, K.J. Dalgaard, M.R. Madsen, M.M. Pohl, E. Welter, P. Lamagni, K.B. Buhl, M. Bremholm, M. Beller, S.U. Pedersen, T. Skrydstrup, K. Daasbjerg, Selective CO2 reduction to CO in water using earth-abundant metal and nitrogen-doped carbon electrocatalysts, ACS Catal. 8 (7) (2018) 6255–6264.
[47] S.H. Lee, J. Kim, D.Y. Chung, J.M. Yoo, H.S. Lee, M.J. Kim, B.S. Mun, S.G. Kwon, Y. E. Sung, T. Hyeon, Design principle of Fe-N-C electrocatalysts: how to optimize multimodal porous structures? J. Am. Chem. Soc. 141 (2019) 2035–2045.
[48] F. Jaouen, M. Lefèvre, J.-P. Dodelet, M. Cai, Heat-treated Fe/N/C catalysts for O_2 electroreduction: are active sites hosted in micropores? J. Phys. Chem. B 110 (11) (2006) 5553–5558.
[49] A. Zitolo, V. Goellner, V. Armel, M.-T. Sougrati, T. Mineva, L. Stievano, E. Fonda, F. Jaouen, Identification of catalytic sites for oxygen reduction in iron- and nitrogen-doped graphene materials, Nat. Mater. 14 (9) (2015) 937–942.
[50] F. Jaouen, M. Lefèvre, J.-P. Dodelet, M. Cai, Heat-treated Fe/N/C catalysts for O_2 electroreduction: are active sites hosted in micropores? J. Phys. Chem. B 110 (11) (2006) 5553–5558.
[51] U.A. Paulus, T.J. Schmidt, H.A. Gasteiger, R.J. Behm, Oxygen reduction on a high-surface area Pt/Vulcan carbon catalyst: a thin-film rotating ring-disk electrode study, J. Electroanal. Chem. 495 (2) (2001) 134–145.
[52] A.V. Neimark, Y. Lin, P.I. Ravikovitch, M. Thommes, Quenched solid density functional theory and pore size analysis of micro-mesoporous carbons, Carbon 47 (7) (2009) 1617–1628.
[53] A.M.P.O.I. Poddubnaya, B.G.M. Sobiesiak, Comparison of Heterogeneous Pore Models QSDFT and 2D-NLDFT and Computer Programs ASiQwin and SAIEUS for Calculation of Pore Size Distribution, 2016, pp. 459–464.
[54] Y. Zhu, J. Gao, Y. Li, F. Sun, J. Gao, S. Wu, Y. Qin, Preparation of activated carbons for SO 2 adsorption by CO 2 and steam activation, J. Taiwan Inst. Chem. Eng. 43 (1) (2012) 112–119.
[55] S. Román, J.F. González, C.M. González-García, F. Zamora, Control of pore development during CO2 and steam activation of olive stones, Fuel Process. Technol. 89 (8) (2008) 715–720.
[56] C.F. Chang, C.Y. Chang, W.T. Tsai, Effects of burn-off and activation temperature on preparation of activated carbon from corn cob agrowaste by CO2 and steam, J. Colloid Interface Sci. 232 (1) (2000) 45–49.
[57] M. Thommes, K. Kaneko, A.V. Neimark, J.P. Olivier, F. Rodriguez-Reinoso, J. Rouquerol, K.S.W. Sing, Physisorption of gases, with special reference to the evaluation of surface area and pore size distribution (IUPAC technical report), Pure Appl. Chem. 87 (9–10) (2015) 1051–1069.
[58] F. Rodríguez-Reinoso, M. Molina-Sabio, M.T. González, The use of steam and CO_2 as activating agents in the preparation of activated carbons, Carbon 33 (1) (1995) 15–23.
[59] M. Molina-Sabio, M.T. González, F. Rodriguez-Reinoso, A. Sepúlveda-Escribano, Effect of steam and carbon dioxide activation in the micropore size distribution of activated carbon, Carbon 34 (4) (1996) 505–509.
[60] F. Rodríguez-Reinoso, M. Molina-Sabio, Activated carbons from lignocellulosic materials by chemical and/or physical activation: an overview, Carbon 30 (7) (1992) 1111–1118.
[61] J. Blackwood, A. Ingeme, The reaction of carbon with carbon dioxide at high pressure, Aust. J. Chem. 13 (2) (1960) 194.
[62] A.C. Lua, J. Guo, Activated carbon prepared from oil palm stone by one-step CO_2 activation for gaseous pollutant removal, Carbon 38 (7) (2000) 1089–1097.
[63] G. Tobias, L. Shao, C.G. Salzmann, Y. Huh, M.L.H. Green, Purification and opening of carbon nanotubes using steam, J. Phys. Chem. B 110 (2006) 22318–22322.
[64] R. Wang, S. Sang, D. Zhu, S. Liu, K. Yu, Pore characteristics and controlling factors of the lower Cambrian Hetang formation shale in northeast Jiangxi, China, Energy Explor. Exploit. 36 (1) (2018) 43–65.
[65] X. Tang, Z. Jiang, Z. Li, Z. Gao, Y. Bai, S. Zhao, J. Feng, The effect of the variation in material composition on the heterogeneous pore structure of high-maturity shale of the Silurian Longmaxi formation in the southeastern Sichuan Basin, China, J. Nat. Gas Sci. Eng. 23 (2015) 464–473.
[66] A.C. Ferrari, Determination of bonding in diamond-like carbon by Raman spectroscopy, Diam. Relat. Mater. 11 (3–6) (2002) 1053–1061.
[67] M. Pawlyta, J.N. Rouzaud, S. Duber, Raman microspectroscopy characterization of carbon blacks: spectral analysis and structural information, Carbon 84 (1) (2015) 479–490.
[68] A. Sadezky, H. Muckenhuber, H. Grothe, R. Niessner, U. Pöschl, Raman microspectroscopy of soot and related carbonaceous materials: spectral analysis and structural information, Carbon 43 (8) (2005) 1731–1742.
[69] V. Perazzolo, C. Durante, R. Pilot, A. Paduano, J. Zheng, G.A. Rizzi, A. Martucci, G. Granozzi, A. Gennaro, Nitrogen and sulfur doped mesoporous carbon as metal-free electrocatalysts for the in situ production of hydrogen peroxide, Carbon 95 (2015) 949–963.
[70] V. Palomares, A. Goñi, I.G. De Muro, I. De Meatza, M. Bengoechea, I. Cantero, T. Rojo, Conductive additive content balance in li-ion battery cathodes: commercial carbon blacks vs. in situ carbon from LiFePO4/C composites, J. Power Sources 195 (22) (2010) 7661–7668.
[71] B.S. Elman, M.S. Dresselhaus, G. Dresselhaus, E.W. Maby, H. Mazurek, Raman scattering from ion-implanted graphite, Phys. Rev. B 24 (2) (1981) 1027–1034.
[72] Y. Wang, D.C. Alsmeyer, R.L. McCreery, Raman spectroscopy of carbon materials: structural basis of observed spectra, Chem. Mater. 2 (5) (1990) 557–563.
[73] L. Bokobza, J.-L. Bruneel, M. Couzi, Raman spectra of carbon-based materials (from graphite to carbon black) and of some silicone composites, C J. Carbon Res. 1 (1) (2015) 77–94.
[74] A.C. Ferrari, J. Robertson, Interpretation of Raman spectra of disordered and amorphous carbon, Phys. Rev. B 61 (20) (2000) 14095–14107.
[75] R. Sparkes, N. Hovius, A. Galy, R.V. Kumar, J.T. Liu, Automated analysis of carbon in powdered geological and environmental samples by Raman spectroscopy, Appl. Spectrosc. 67 (7) (2013) 779–788.
[76] R. Chenitz, U.I. Kramm, M. Lefèvre, V. Glibin, G. Zhang, S. Sun, J.P. Dodelet, A specific demetalation of Fe-N4 catalytic sites in the micropores of NC-Ar + NH3 is at the origin of the initial activity loss of the highly active Fe/N/C catalyst used for the reduction of oxygen in PEM fuel cells, Energy Environ. Sci. 11 (2) (2018) 365–382.
[77] M. Blanco, D. Mosconi, M. Otyepka, M. Medveď, A. Bakandritsos, S. Agnoli, G. Granozzi, Combined high degree of carboxylation and electronic conduction in graphene acid sets new limits for metal free catalysis in alcohol oxidation, Chem. Sci. 10 (41) (2019) 9438–9445.
[78] D. Mosconi, M. Blanco, T. Gatti, L. Calvillo, M. Otyepka, A. Bakandritsos, E. Menna, S. Agnoli, G. Granozzi, Arene C e H insertion catalyzed by ferrocene covalently heterogenized on graphene acid, Carbon 143 (2019) 318–328.
[79] G. Levi, O. Senneca, M. Causà, P. Salatino, P. Lacovig, S. Lizzit, Probing the chemical nature of surface oxides during coal char oxidation by high-resolution XPS, Carbon 90 (2015) 181–196.
[80] S. Pylypenko, S. Mukherjee, T.S. Olson, P. Atanassov, Non-platinum oxygen reduction electrocatalysts based on pyrolyzed transition metal macrocycles, Electrochim. Acta 53 (27) (2008) 7875–7883.
[81] S. Hu, M. Tian, E.L. Ribeiro, G. Duscher, D. Mukherjee, Tandem laser ablation synthesis in solution-galvanic replacement reaction (LASiS-GRR) for the production of PtCo nanoalloys as oxygen reduction electrocatalysts, J. Power Sources 306 (2016) 413–423.
[82] V. Perazzolo, E. Grądzka, C. Durante, R. Pilot, N. Vicentini, G.A. Rizzi, G. Granozzi, A. Gennaro, Chemical and electrochemical stability of nitrogen and sulphur doped mesoporous carbons, Electrochim. Acta 197 (2016) 251–262.
[83] A. Bonakdarpour, M. Lefevre, R. Yang, F. Jaouen, T. Dahn, J.-P. Dodelet, J.R. Dahn, Impact of loading in RRDE experiments on Fe–N–C catalysts: two- or four-electron oxygen reduction? Electrochem. Solid-State Lett. 11 (6) (2008) B105.
[84] S. Kabir, K. Artyushkova, B. Kiefer, P. Atanassov, Computational and experimental evidence for a new TM-N3/C moiety family in Non-PGM electrocatalysts, Phys. Chem. Chem. Phys. 17 (27) (2015) 17785–17789.
[85] D. Malko, A. Kucernak, T. Lopes, Performance of Fe–N/C oxygen reduction electrocatalysts toward NO_2–, NO, and NH_2OH electroreduction: from fundamental insights into the active center to a new method for environmental nitrite destruction, J. Am. Chem. Soc. 138 (49) (2016) 16056–16068.
[86] S. Specchia, P. Atanassov, J.H. Zagal, Mapping transition metal-nitrogen-Carbon catalysts performance on the critical descriptors diagram, Curr. Opin. Electrochem. (2021), 100687, https://doi.org/10.1016/j.coelec.2021.100687.
[87] S.H. Liu, J.R. Wu, F.S. Zheng, J.M. Guo, Impact of iron precursors on the properties and activities of carbon-supported Fe-N oxygen reduction catalysts, J. Solid State Electrochem. 19 (2015) 1381–1391, https://doi.org/10.1007/s10008-015-2759-1.